Abundant sub-micron grains revealed in newly discovered extreme debris discs

Attila Moór,[1,2]★ Péter Ábrahám,[1,2,3,7] Kate Y. L. Su,[4] Thomas Henning,[5] Sebastian Marino,[6] Lei Chen,[1,2] Ágnes Kóspál,[1,2,5,3] Nicole Pawellek,[7,1,2] József Varga,[1,2] Krisztián Vida,[1,2]

[1]*Konkoly Observatory, Research Centre for Astronomy and Earth Sciences, HUN-REN, Konkoly-Thege Miklós út 15-17, H-1121 Budapest, Hungary*
[2]*CSFK, MTA Centre of Excellence, Budapest, Konkoly Thege Miklós út 15-17., H-1121, Hungary*
[3]*ELTE Eötvös Loránd University, Institute of Physics, Pázmány Péter sétány 1/A, H-1117 Budapest, Hungary*
[4]*Department of Astronomy/Steward Observatory, The University of Arizona, Tucson, AZ 85721-0009, USA*
[5]*Max-Planck-Institut für Astronomie, Königstuhl 17, D-69117 Heidelberg, Germany*
[6]*Department of Physics and Astronomy, University of Exeter, Stocker Road, Exeter EX4 4QL, UK*
[7]*Department of Astrophysics, University of Vienna, Türkenschanzstraße 17, 1180, Vienna, Austria*

Accepted XXX. Received YYY; in original form ZZZ

ABSTRACT

Extreme debris discs (EDDs) are bright and warm circumstellar dusty structures around main sequence stars. They may represent the outcome of giant collisions occuring in the terrestrial region between large planetesimals or planetary bodies, and thus provide a rare opportunity to peer into the aftermaths of these events. Here, we report on results of a mini-survey we conducted with the aim to increase the number of known EDDs, investigate the presence of solid-state features around 10 μm in eight EDDs, and classify them into the silica or silicate dominated groups. We identify four new EDDs and derive their fundamental properties. For these, and for four other previously known discs, we study the spectral energy distribution around 10 μm by means of VLT/VISIR photometry in three narrow-band filters and conclude that all eight objects likely exhibit solid-state emission features from sub-micron grains. We find that four discs probably belong to the silicate dominated subgroup. Considering the age distribution of the entire EDD sample, we find that their incidence begins to decrease only after 300 Myr, suggesting that the earlier common picture that these objects are related to the formation of rocky planets may not be exclusive, and that other processes may be involved for older objects ($\gtrsim$100 Myr). Because most of the older EDD systems have wide, eccentric companions, we suggest that binarity may play a role in triggering late giant collisions.

Key words: (stars:) circumstellar matter – infrared: planetary systems – stars: individual: TYC 5940-1510-1, TYC 8105-310-1, TYC 4946-1106-1, J060917.00-150808.5, J071206.54-475242.3, J092521.90-673224.8, J104416.70-451613.9, J204315.23+104335.3

1 INTRODUCTION

In recent decades, observations at mid-infrared (mid-IR) wavelengths have led to the identification of a number of main-sequence stars surrounded by warm dust at temperatures of ~200–600 K (e.g., Kennedy & Wyatt 2013; Cruz-Sáenz de Miera et al. 2014; Cotten & Song 2016). For Sun-like stars with a spectral type between mid F and late K, these temperatures are indicative of dust grains located within a few au, i.e. in a region where the terrestrial planets orbit in the Solar System. The lifetime of such small warm particles is significantly shorter than the age of their host star, as under the influence of stellar radiation and stellar wind they are removed from the system on a timescale of tens of thousands of years at most. So the long-term maintenance of a circumstellar disc requires continuous dust replenishment from erosion of larger bodies. The second generation debris grains could either be released from an in situ collisional cascade that grinds a ring of planetesimals into (sub)micron-sized particles, from a single large collision, or even from bodies originally located much further away, for example as sublimation or disruption of icy minor bodies transported from a cold, outer reservoir into the inner region (Wyatt 2008; Rigley & Wyatt 2022).

Some warm debris discs contain such large amounts of dust that are clearly not sustainable for the lifetime of the system, implying instead that a recent episodic dust production event has resulted in a strongly elevated dust level for a temporary period (Wyatt et al. 2007). The IR luminosity of the dustiest of these warm transient discs exceeds 1% of the luminosity of their host stars. These so-called extreme debris discs (EDDs), of which we currently know about 20 (Oudmaijer et al. 1992; Gorlova et al. 2004; Song et al. 2005; Gorlova et al. 2007; Rhee et al. 2008; Melis et al. 2010; Zuckerman et al. 2012; de Wit et al. 2013; Tajiri et al. 2020; Melis et al. 2021; Moór et al. 2021; Higashio et al. 2022), are pro-

★ E-mail: moor.attila@csfk.org

posed to be signatures of giant impacts during the final assembly of rocky planets, or the outcome of a late dynamical instability of a planetary system, or of a collision between a rocky planet and its former moon that became unbound due to tidal evolution (Melis 2016; Su et al. 2019; Moór et al. 2021; Melis et al. 2021; Hansen 2023).

Mid-IR spectroscopic observations between 5 and 35 μm with the Infrared Spectrograph (IRS; Houck et al. 2004) onboard the *Spitzer* Space Telescope (*Spitzer*; Werner et al. 2004) revealed several warm debris discs with solid state emission features that can mostly be attributed to small silicate particles with sizes from submicron to a few μm (e.g., Ballering et al. 2014; Mittal et al. 2015). Position and shape of the observed features allow us to study the crystalline fraction and mineralogy of dust which can provide insights into the composition of the parent bodies (the outer layers for larger objects) and can help to constrain the processes that led to the dust release (Henning 2010; Lisse et al. 2008, 2012; Olofsson et al. 2012). Spectra with the most prominent features tend to be displayed by bright transient debris discs. By analysing the IRS data of 12 debris discs, most having transient nature, Morlok et al. (2014) found that basically two groups can be distinguished. For a subset of discs, the most dominant feature peaks between 9 and 9.5 μm indicating the presence of silica grains (e.g. quartz, cristobalite, silica glass, Koike et al. 2013), while for the other subset, the spectra are charaterized by strong features peaking in the 9.9–11.3 μm wavelength range, suggesting dust material dominated by silicate particles (e.g. pyroxene, olivine, Henning 2010). By comparing these spectra with those of terrestrial and Martian rocks, they argued that the former subset is more similar to crustal material, while the latter has features more akin to mantle-type samples. Assuming that the source of the observed debris dust was a collision between differentiated planetary bodies, the above comparison gives an indication of the portion of the planet from which the ejected material originated and can also provide a constraint on the nature of the collision (Morlok et al. 2014).

EDDs offer a direct view at the aftermaths of large collisions. Here we present a study, whose aim was to gain a deeper understanding of this phenomenon. First we focus on increasing the available EDD sample, and report on the discovery of four new EDDs. Then we supplement the newly discovered sources with four already known objects, and perform a mini-survey using the VLT/VISIR camera to obtain multi-band mid-IR photometry for eight EDDs, with the aim to investigate whether they also show solid-state features around 10 μm, and which of the above subgroups they are more likely to belong to. The novelty of this project is that before 2009, when the primary "cold" mission of the *Spitzer* stopped, and thus the IRS ceased to operate, only a handful of EDDs were known. Although some of the brightest objects identified since 2009 have been observed by means of ground-based mid-IR spectroscopy in the 8–13 μm range, only half of the currently known EDDs have mid-IR spectroscopic data. Our survey provides narrow-band photometry for sources which would otherwise be too faint for ground-based spectroscopy, this way significantly increasing the sample of EDDs with information on the 10 μm feature.

Basic properties of the newly discovered EDDs are derived and presented in Sect. 2. The mid-IR spectroscopic observations and data reduction are summarized in Sect. 3. The results are presented in Sect. 4 and their implication are discussed in Sect. 5. Finally, in Sect. 6, the main outcomes of our investigation are summarized.

Table 1. Log of spectroscopic observations.

AllWISE / Gaia DR3 name	Obs. date	Programme ID
J060917.00−150808.5	2021-02-13	0106.A-9012(A)
J071206.54−475242.3	2021-02-14	0106.A-9012(A)
J092521.90−673224.8	2012-12-25	090.C-0815(A)
	2022-06-08	0109.A-9029(A)
J104416.70−451613.9	2021-02-13	0106.A-9012(A)
Gaia DR3 5366814012930376960	2021-02-13	0106.A-9012(A)
J204315.23+104335.3	2022-06-09	0109.A-9029(A)

2 PROPERTIES OF THE NEWLY DISCOVERED EDDS

We have been carrying out a long term project whose aim is to identify and investigate EDDs around Sun-like stars located within 400 pc using a combined data set, based on the AllWISE mid-IR photometric (Wright et al. 2010) and Gaia Data Release 3 (Gaia DR3, Gaia Collaboration et al. 2023) astrometric catalogues. All details of the identification process will be described in a subsequent paper (Moór et al. in prep.). For our photometric survey, we selected four, yet unpublished objects from our comprehensive EDD list, J060917.00−150808.5 (hereafter J060917), J071206.54−475242.3 (J071206), J104416.70−451613.9 (J104416), and J204315.23+104335.3 (J204315), on the basis of their mid-IR brightness and observability from the southern hemisphere.

The four newly discovered EDDs are complemented by four recently identified objects from the literature. TYC 5940-1510-1 (TYC 5940), TYC 8105-370-1 (TYC 8105), and TYC 4946-1106-1 (TYC 4946) are those three of the six new EDDs presented in Moór et al. (2021) that are observable from Cerro Paranal, while J092521.90-673224.8 (J092521) is taken from Higashio et al. (2022).

In the following, we derive fundamental stellar and disc properties of the four newly discovered EDDs and J092521. Similar data for TYC 5940, TYC 8105, and TYC 4946 can be found in Moór et al. (2021).

2.1 Fundamental stellar properties

To estimate fundamental stellar properties of the four newly discovered EDDs and J092521 we obtained their high resolution (R = 48 000) optical spectra using the Fibre-fed Extended Range Optical Spectrograph (FEROS, Kaufer et al. 1999) mounted on ESO/MPG 2.2 m telescope at La Silla Observatory (Chile). The observations were executed in three different projects (090.C-0815(A) – PI: Attila Moór, 0106.A-9012(A) – PI: Sebastian Marino, and 0109.A-9029(A) – PI: Thomas Henning). In all measurements we used the object-sky observing mode in which one of the two fibres targeted the star while the other was positioned at the sky. The log of observations is given in Table 1. The data reduction of the obtained spectra was carried out utilizing the CERES (Collection of Elemental Routines for Echelle Spectra) pipeline developed by Brahm et al. (2017a).

We employed the ZASPE tool (Zonal Atmospheric Stellar Parameters Estimator, Brahm et al. 2017b) to derive stellar atmospheric parameters, the effective temperature ($T_{\rm eff}$), metallicity ([Fe/H]), surface gravity ($\log g$) using the obtained continuum normalized spectra. For estimating these parameters, ZASPE compares the observed spectrum with a grid of synthetic stellar atmospheric models using least squares minimization. The best fit atmospheric param-

eters as well as the projected rotational velocities ($v \sin i$) and radial velocities ($v_{\rm rad}$) of the EDD host stars yielded by this approach are listed in Table 2. For J092521, the weighted averages of the parameters obtained from its two measurements are presented in the table. J104416 has a wide companion star of similar brightness (Gaia DR3 5366814012930376960, Sect. 2.3), that we also observed with FEROS (Tab. 1) and whose parameters were determined according to the method described above. The value for the metallicity of J104416 in Table 2 is the weighted average of the results for the two stars. In addition to the fundamental stellar properties, Table 2 also shows alternative identifiers, astrometric and photometric data, as well as galactic space position and velocity of the targets.

2.2 Equivalent width of the Li I line

Using the continuum normalized FEROS spectra we determined the equivalent width of the Li I line. To this end, the two Li I components at 6707.761 Å and at 6707.912 Å and the very nearby Fe I line at 6707.431 Å were fitted as a combination of three Gaussians. The obtained EWs are listed in Table 2.

2.3 Multiplicity

Data available in the Gaia DR3 catalogue, supplemented by our spectroscopic results allow us to search for possible companion stars of our targets located at different separations, from close spectroscopic binaries to the widest pairs. By examining cross correlation function (CCF) profiles calculated from our high resolution spectra we found no indication that any of the host stars of are double-lined spectroscopic binaries. RV data for all targets, except J092521, are available in the Gaia DR3 catalogue and are in good agreement with the radial velocities obtained from FEROS observations (the RV differences are in all cases less than 1.5× the uncertainty of the difference, see Table 2). For J092521, we have FEROS data for two epochs (Table 1) and the RV velocities obtained are in perfect agreement. The RV values reported in DR3 catalogue are a combination of all individual measurements performed in the first 34 months of the observing mission (Katz et al. 2023). Although the measured radial velocity time series are currently published only for a limited number of objects, the catalogue already includes two indices (`rv_chisq_pvalue` and `rv_renormalised_gof`, Katz et al. 2023) that can be used to identify RV variability for stars with 3900 K < `rv_template_teff` < 8000K, that are sufficiently bright (`grvs_mag` < 12 mag) and have been observed at least ten times. Since these indices became available in the DR3 release, we investigated possible RV variability for all systems targeted in our project, with the exception of J092521, for which there are no RV data in the catalogue. We found that TYC 5940 fulfills the criteria (`rv_chisq_pvalue`<0.01 and `rv_renormalised_gof`>4) recommended by Katz et al. (2023) and thus exhibits significant RV variability raising the possibility that it has a close companion. However, we note that our ground-based radial velocity measurement for the star (+28.50±0.20 km s^{-1}, Moór et al. 2021) is in good agreement with the mean RV data listed in the Gaia DR3 catalogue (+27.82±1.05 km s^{-1}), which does not indicate any significant change.

The re-normalized unit weight error (`ruwe`) indicates the quality of the applied astrometric solution which is based on a single-star model (Lindegren et al. 2021). A `ruwe` value greater than 1.4 implies a potentially unreliable astrometric solution (Fabricius et al. 2021), which in most cases, although not exclusively (e.g., Fitton et al. 2022), may be due to the presence of an unresolved close companion star located within $\lesssim 1''$. In fact, according to several works (e.g., Belokurov et al. 2020; Bryson et al. 2020; Wolniewicz et al. 2021), unresolved binarity is suspected already at `ruwe` above 1.2. In the light of these results, the high `ruwe` of 12.3 for J071206 is a strong indication that the star may be an unresolved pair, while the `ruwe`=1.24 listed for J092521 suggests only tentatively the presence a companion. However, for the latter the large value of the `ipd_frac_multi_peak` metric (21, Gaia DR3) – that measures what fraction of observing windows where multiple peaks are detected – further strengthens that the source may not be single (Fabricius et al. 2021).

To reveal possible wide companions of the targets we looked for co-moving and co-distant stars in their vicinity using the method proposed by Deacon & Kraus (2020). Only objects with `ruwe`<1.4 and $\pi/\sigma_\pi > 4$ (where π and σ_π are the measured parallax and its uncertainty) were considered in the search, and we set a maximum projected separation of 30000 au for the possible companions to avoid binary candidate likely to be chance alignments only (El-Badry et al. 2021). We have found potential wide companions to three stars, J060917, J104416, and J204315. The most important Gaia astrometric parameters along with the projected separations of these pairs are summarised in Table 3. We note that for the target Gaia DR3 5366814012930376960, the pair of J104416, radial velocity is also available in the catalogue, and the quoted RV value of 17.12 ± 0.37 km s^{-1} is in very good agreement with that of J104416 (Table 2), further confirming that the two stars constitute a binary. While for J060917 and J204315, the companions are fainter than the discs' host stars, Gaia DR3 5366814012930376960 is brighter than J104416, implying that in this system the revealed companion is the primary component. The very faint J060917 B is not, but the other two pairs are listed in the wide binary catalogue compiled by El-Badry et al. (2021).

For Gaia DR3 5366814012930376960 we used the ZASPE code to derive its fundamental stellar properties from its high-resolution FEROS spectrum (Sect. 2.1) and obtained the following results: $T_{\rm eff}$ = 5497±78 K, log g = 4.43±0.13, [Fe/H] = -0.26±0.04 (weighted average of the [Fe/H] estimates for Gaia DR3 5366814012930376960 and J104416), $v \sin i$ = 1.77±0.85 km s^{-1}, and $v_{\rm rad}$ = 17.06±0.01 km s^{-1}. We derived a luminosity of 0.575±0.033 L$_\odot$ for the star and <10 mÅ for its lithium EW.

To estimate the effective temperature and spectral type of J204315 B we used its $r - z$, $r - J$, and $G_{BP} - G_{RP}$ colour indices and the method proposed by Mann et al. (2015). The r and z band photometry were taken from the Pan-STARRS Survey (DR1, Chambers et al. 2016) and were transformed into the SDSS system utilizing the equations presented in Tonry et al. (DR1, 2012). The J band data were extracted from the 2MASS survey (Skrutskie et al. 2006), while $G_{BP} - G_{RP}$ colors were from the Gaia DR3 catalogue. Since J204315 has negligible reddening (Sect. 2.4), in this analysis we adopted E(B-V) = 0 for the companion too. The obtained $T_{\rm eff}$ was then used to estimate the spectral type of J204315 B based on the online database[1] of stellar parameters of dwarf stars (Pecaut & Mamajek 2013). The spectral type of J060917 B, where reliable photometry was available only in the G band, was estimated based on its M_G absolute magnitude by interpolating in the same database. In estimating the parameters of J204315 B and J060917 B, the distance of their primary component has been adopted (Table 2). The derived stellar parameters of the companions are quoted in Table 3.

[1] https://www.pas.rochester.edu/~emamajek/EEM_dwarf_UBVIJHK_colors_Teff.txt

Table 2. Properties of newly discovered EDD systems. References: 1 - Cutri & et al. (2014), 2 - Gaia DR3, 3 - Høg et al. (2000), 4 - Cutri et al. (2003), 5 - Henden et al. (2016), 6 - Bailer-Jones et al. (2021), 7 - This work.

Parameters	J060917	J071206	J092521	J104416	J204315	Ref.
			Identifiers			
AllWISE	J060917.00−150808.5	J071206.54−475242.3	J092521.90−673224.8	J104416.70−451613.9	J204315.23+104335.3	1
Gaia DR3	2993153951148830336	5508896788120942848	5247128354025136128	5366813974272886528	1751335969361640192	2
TYCHO	-	-	9196-2916-1	-	-	3
2MASS	06091701−1508085	07120655−4752423	09252194−6732251	10441680−4516142	20431522+1043355	4
			Astrometric data			
R.A. (2000)	06:09:17.011	07:12:06.544	09:25:21.973	10:44:16.798	20:43:15.223	2
Decl (2000)	−15:08:08.59	−47:52:42.36	−67:32:25.06	−45:16:14.36	+10:43:35.60	2
$\mu_\alpha \cos\delta$ (mas)	−6.271±0.011	−8.606±0.154	−17.794±0.021	−89.291±0.009	+12.996±0.015	2
μ_δ (mas)	+0.882±0.012	−2.096±0.159	+25.950±0.022	+29.754±0.010	−15.934±0.013	2
π (mas)	2.832±0.013	5.751±0.125	10.106±0.020	5.007±0.011	8.479±0.014	2
`ruwe`	0.96	12.27	1.24	0.91	0.99	2
			Photometric data			
B	14.34±0.05	13.92±0.05	13.04±0.04	12.94±0.06	13.27±0.04	5
V	13.54±0.05	12.85±0.01	11.92±0.02	12.20±0.01	12.26±0.05	5
G_{BP}	13.7431±0.0039	13.0773±0.0035	12.1514±0.0032	12.6394±0.0028	12.4620±0.0032	2
G_{RP}	12.7325±0.0042	11.7441±0.0040	10.7075±0.0047	11.6415±0.0038	11.1882±0.0040	2
G	13.3206±0.0029	12.5031±0.0030	11.5499±0.0028	12.2222±0.0028	11.8971±0.0028	2
J	12.058±0.023	10.821±0.024	9.733±0.026	10.946±0.036	10.366±0.023	4
H	11.643±0.022	10.296±0.027	9.174±0.026	10.540±0.034	9.824±0.028	4
K_s	11.481±0.023	10.176±0.025	9.004±0.024	10.460±0.030	9.679±0.023	4
			Kinematics and positions			
$v_{\rm rad}$ **(km s^{-1})**	+23.44±2.32	+27.64±1.10	-	+17.56±0.55	−20.30±0.52	2
	+20.16±0.03	+28.57±0.13	+18.89±0.14	+17.18±0.04	−19.47±0.22	7
U (km s^{-1})	−16.34±0.03	−6.02±0.13	−9.06±0.05	−82.26±0.17	−9.45±0.11	7
V (km s^{-1})	−7.17±0.04	−24.61±0.14	−22.15±0.13	−35.92±0.06	−20.25±0.16	7
W (km s^{-1})	−14.05±0.05	−15.06±0.19	−1.43±0.03	−11.84±0.03	−3.99±0.07	7
X (pc)	−248.69±1.26	−32.55±0.67	+25.22±0.05	+36.01±0.07	+61.59±0.10	7
Y (pc)	−224.11±1.13	−163.87±3.40	−93.32±0.17	−191.37±0.38	+92.48±0.15	7
Z (pc)	−96.20±0.49	−49.57±1.03	−20.75±0.04	+41.50±0.08	−38.19±0.06	7
Distance (pc)	$348.3^{+1.8}_{-1.7}$	$174.3^{+3.2}_{-4.1}$	98.9±0.2	$199.1^{+0.3}_{-0.5}$	117.5±0.2	6
			Stellar properties			
Spectral type	G9V	K3.5V	K4.5V	K0.5V	K4V	7
$T_{\rm eff}$ (K)	5409±52	4682±69	4513±49	5241±68	4642±59	7
[Fe/H] (dex)	−0.02±0.03	−0.20±0.06	−0.23±0.04	−0.35±0.05	−0.15±0.05	7
log g (dex)	4.56±0.08	4.48±0.13	4.43±0.11	4.48±0.08	4.48±0.11	7
$E(B-V)$	0.058±0.017	0.025±0.014	0.0±0.015	0.010±0.014	0.0±0.016	7
L_* ($L_\odot$)	0.493±0.019	0.284±0.017	0.224±0.010	0.406±0.021	0.207±0.011	7
R_* ($R_\odot$)	0.80±0.02	0.84±0.04	0.81±0.02	0.77±0.03	0.70±0.03	7
M_* ($M_\odot$)	0.90±0.01	0.69±0.02	$0.65^{+0.03}_{-0.02}$	0.83±0.02	0.72±0.01	7
$v \sin i_*$ (km s^{-1})	2.13±0.70	3.68±0.89	0.90±0.76	0.70±0.73	3.18±0.93	7
$P_{\rm rot}$ (day)	6.55±0.08	8.55±0.17	4.95±0.05	-	9.0±0.2	7
Li I EW (mÅ)	143±5	<21	108±2	<11	35±4	7
Age (Myr)	208^{+104}_{-65}	243^{+91}_{-77}	85^{+49}_{-28}	5500^{+2400}_{-2200}	252^{+80}_{-65}	7
Multiplicity	Yes	Likely	?	Yes	Yes	7
			Disc properties			
$T_{\rm d}$ (K)	752±48 / 237±22[a]	434±25	857±90 / 99±6[a]	405±21	404±15	7
$f_{\rm d}$[b]	0.075/0.027[a]	0.026	0.021/0.033[a]	0.025	0.048	7
$R_{\rm BB}$ (au)	0.1/0.97	0.22	0.05/3.7	0.30	0.22	7
mid-IR var.	Y	N	Y	N	Y	7

[a] Spectral energy distributions of excess emission of J061709 and J092521 are fitted with two-temperature blackbody models (Sect. 2.7.2).
[b] f_d is the fractional luminosity ($f_d = L_{\rm disc}/L_*$).

Table 3. Astrometric parameters and stellar properties of the probable common motion and distance pairs.

Gaia DR3 id	Pair	Separation ($''$/au)	$\mu_\alpha \cos\delta$ (mas)	μ_δ (mas)	π (mas)	G (mag)	SpT	$T_{\rm eff}$ (K)	M_G (mag)
2993153951145272192	J060917	1.″96/682	−4.421±0.589	+0.554±0.721	3.527±0.775	20.103±0.009	M4.5	-	12.286±0.039
5366814012930376960	J104416	51.″56/10261	−89.165±0.011	+29.954±0.012	4.995±0.013	11.843±0.003	G8V	5497±78	5.295±0.027
1751335969361640576	J204315	18.″96/2228	+12.556±0.039	−16.459±0.039	8.508±0.037	15.733±0.003	M3.5	3244±48	10.383±0.016

2.4 Stellar photosphere models

To estimate the stellar luminosity and the reddening as well as to predict the photospheric contribution to the total flux at IR wavelengths, the optical and near-IR spectral energy distributions (SEDs) of the stars were fitted by ATLAS9 atmosphere models (Castelli & Kurucz 2004). The broadband photometric data, utilized in the modelling, were taken from the APASS (AAVSO Photometric All-Sky Survey Henden et al. 2016), TYCHO2 (Høg et al. 2000), Gaia DR3, and 2MASS (Two Micron All Sky Survey, Cutri et al. 2003) catalogues. From the latter data set, only the J- and H-band photometry was used, as because of the presence of warm dust, the possibility of some IR excess even in the K-band cannot be excluded. In the case of J092521, the Gaia $B_{\rm P}$ and $R_{\rm P}$ data were also discarded, because the corrected $B_{\rm P}$ and $R_{\rm P}$ flux excess factor (Riello et al. 2021) suggests a significant inconsistency between photometry in these bands with respect to G-band data. To account for possible interstellar reddening we adopted the extinction law from Fitzpatrick (1999). In the course of fitting we used a grid-based approach. In the first step the $\log g$, and [Fe/H] parameters of the atmospheric model were fixed to the best-fit values derived in our spectroscopic analysis, but $T_{\rm eff}$ was free to vary. For J060917, J104416, and J204315, the obtained best fit $T_{\rm eff}$ values were in agreement with the estimates derived from the spectral analysis within 30 K. In these cases, we finally fixed the effective temperatures to the latter values and repeated the photospheric fitting. For J071206 and J092521, the fitting resulted in models with temperatures of 80 and 90 K lower, respectively, than the ones obtained from the analysis of their spectra. One possible explanation for this is that these two objects may have fainter, cooler companions – as suggested by their Gaia data (Sect. 2.3) – that also contribute to the total measured flux in all available photometric bands. For these sources, therefore, we kept the resulting colder photospheric models. The luminosities (L_*) and reddenings (E(B-V)) obtained by the fitting are given in Table 2. We note that the resulting E(B-V) values are in good agreement with the ones that can be extracted for our targets from the Stilism 3D reddening map[2] (Capitanio et al. 2017; Lallement et al. 2018).

2.5 Optical variability

Our targets are G9–K4.5 type stars, they are likely magnetically active, thus, they may be spotted, which leads to rotational modulation in their light curves. To search for possible modulation and to determine the stellar rotational periods we studied the optical variability of our targets using photometric observations obtained by the Transiting Exoplanet Survey Satellite (TESS, Ricker et al. 2015) and in the ground based All-Sky Automated Survey for Supernovae (ASAS-SN, Shappee et al. 2014; Kochanek et al. 2017) project. The data taken by ASAS-SN are also useful to investigate possible longer-term trend-like variations in the brightness of stars, which may be important in determining whether the variability seen in the mid-IR is related to discs or not (Sect. 2.7.3).

2.5.1 *TESS observations*

All five EDD host stars in Table 2, as well as Gaia DR3 5366814012930376960, the companion of J104416, were observed by the TESS in the full-frame image (FFI) mode, enabling us to investigate their variations on daily/weekly timescales, including rotational modulations, with a high precision. Table 4 shows the TESS Input Catalog (TIC) identifiers of our targets along with the information in which TESS Sectors they were measured. While during the TESS primary mission (S1-S26) the full frame images were acquired at a 30-minute cadence, later, in the extended mission a shorter 10-minute cadence was used. In our analysis, we used un-detrended light-curves extracted by the MIT Quick Look Pipeline (Huang et al. 2020a,b; Kunimoto et al. 2021, 2022) from the FFI images using simple aperture photometry. These data were downloaded from the Mikulski Archive for Space Telescopes (MAST[3]). J204315 was only observed in one sector, and 46% of its light curve are flagged as having bad quality by the QLP pipeline (because of straylight from Earth or Moon in camera FOV and/or low precision). Therefore, this measurement was not included in the analysis. To search for periodic changes in the other light curves we constructed their periodograms using the Generalized Lomb-Scargle algorithm (GLS, Zechmeister & Kürster 2009) utilizing its implementation in PyAstronomy[4] (Czesla et al. 2019). The periodograms were calculated separately for each ∼27 d long sectors. No significant periodic variation was found for J104416 and Gaia DR3 5366814012930376960. J071206 and J092521 show periodic modulation in all six sectors in which they were observed. We selected the most significant peaks in each sector, and the final period and its uncertainty was computed as the average and standard deviation of the individual results. This approach yielded periods of 8.55±0.17 d and 4.95±0.05 d for J071206 and J092521, respectively. For J060917 we also found a significant peak at 6.55±0.08 days in the periodogram. The amplitudes of the detected modulations range between $0.^{\rm m}001$ and $0.^{\rm m}008$.

2.5.2 *ASAS-SN observations*

Our targets were also covered by the ASAS-SN providing V-band photometry between 2012 and 2018 and g-band data since 2018. To compile the light curves we used the `Sky Patrol` tool[5]. After

[2] https://stilism.obspm.fr

[3] https://mast.stsci.edu

[4] https://github.com/sczesla/PyAstronomy

[5] https://asas-sn.osu.edu/

Table 4. TESS observations

Name	TIC identifier	Sectors
J060917	TIC 408967891	S33
J071206	TIC 134435629	S6–8, S33–35
J092521	TIC 304170889	S9–11, S36-38
J104416	TIC 146890996	S9–10, S36
Gaia DR3 5366814012930376960	TIC 146890957	S9–10,S36
J204315	TIC 282627688	S55

removing longer term trends from these data using a LOWESS algorithm, we calculated GLS periodograms for the detrended light curves. For J071206, a significant peak was found in the V and g band measurements with periods of 8.67 and 8.61 days respectively, which is in good agreement with the 8.55 d period found in the TESS dataset. The case of J204315 is similar, we found periodic signals in both light curves with a period of 9.06±0.12 d in the V-band and a period of 8.88±0.16 d in the g-band. In our analysis we will use the weighted average of the two results is 9.0±0.1 d.

The derived rotational periods are listed in Table 2.

2.6 Stellar ages

Our age estimates for stars are mainly based on the rotation-age (gyrochronology, Barnes 2003) and lithium depletion-age relationships, although in some cases kinematic information and position on the HRD were also considered. Figure 1 shows the rotation periods (left panel) – where available (Sect. 2.5) – and the lithium equivalent width (right panel) of the stars as a function of effective temperature. Similar data of single stars belonging to nearby moving groups and open clusters of different ages are also plotted. A comparison with these well-dated objects gives an immediate rough estimate on the age of our stars. To quantify the best age estimate and its uncertainty, we applied the `gyro-interp` (Bouma et al. 2023) and `eagles` (Estimating AGes from Lithium Equivalent widthS, Jeffries et al. 2023) tools. Both packages use empirical models calibrated with measurements of stars in clusters of known age and provide posterior age probability distributions. The `gyro-interp` uses the effective temperature and the rotation period, while the `eagles` the effective temperature and the lithium equivalent width as input parameters. The obtained posteriors were multiplied and the median age and the 68% confidence interval were calculated using the final distribution.

For J060917 and J204315, the combined posteriors yielded age estimates of 208^{+104}_{-65} Myr and 252^{+80}_{-65} Myr, respectively. The latter star has a wide companion at an angular separation of ∼19″ (Sect. 2.3). We compared the position of this M3.5-type star with those of M-type members of various well-dated associations and open clusters on a M_G vs. $G - R_p$ colour-magnitude diagram provided by Popinchalk et al. (2021) (their figure 8). The figure clearly distinguishes M-type stars younger than 50 Myr from those between 100 and 750 Myr, with J204315 B falling into the latter sample, consistently with our age estimate for the primary component.

In the case of J071206, the obtained upper limit on the lithium equivalent width indicates a 95 per cent lower limit of 250 Myr for its age. For this star, the high `ruwe` value and the high luminosity relative to its temperature indicate the presence of a companion that is likely located within ∼1″. Assuming that the observed periodic modulation is related to the rotation of J071206 and not to the putative fainter companion, the `gyro-interp` tool suggests a slightly younger age of 230^{+100}_{-70} Myr. By combining the two posteriors we obtained a final estimate of 243^{+91}_{-77} Myr. Interestingly, the galactic space location and motion of J071206 resembles that of the recently revelead Crius 228 group (Moranta et al. 2022). Moreover, the estimated age of the group (231±35 Myr) is consistent with that of the star (Appendix:A). Together, these seem to be a strong indication for group membership, but it should be kept in mind that the high `ruwe` also implies more uncertain astrometric parameters. Future Gaia data releases may be able to separate the two components or provide an astrometric solution considering the likely non-single nature of this system. Therefore, in the present work we will use the age derived from the stellar data alone.

J092521 is the youngest system in the sample, with its lithium and rotation data together giving an age estimate of 85^{+49}_{-28} Myr. It is also worth evaluating whether the star belongs to any known young kinematic assemblages. Based on the Gaia DR3 astrometric parameters and our radial velocity measurement (Table 2), the `BANYAN Σ` online tool[6] (Gagné et al. 2018) – which is designed to identify possible members in 27 nearby young stellar associations – found a membership probability of 13% to the ∼15 Myr old Lower Centaurus Crux (LCC) subgroup of the Scorpio-Centaurus association and 87% to field. On top of the low probability obtained in the `BANYAN Σ` model, there are further counter-arguments to LCC membership: our estimate indicates a substantially older age and in accordance with this, the star's luminosity is 30% lower than even the faintest K-type LCC member with similar temperatures (4400–4600 K, Pecaut & Mamajek 2016, considering the new Gaia DR3 based distances of the members in the luminosity calculations). Higashio et al. (2022) also argues that J092521 is a young star, and noted that while its velocity is more consistent with membership in the Tucana-Horologium association, its position is closer to the Columba and Carina moving groups. With regard to the latter two groups, it is worth noting that, as Gagné et al. (2021) has recently proposed, they, together with Theia 113 and Theia 208 groups and part of Theia 92 (the latter three are identified by Kounkel & Covey 2019), may constitute the tidal tail of the Platais 8 open cluster. To study the possible membership of J092521 further, we collected the members of the above-mentioned groups from the literature (Booth et al. 2021; Gagné et al. 2018; Gagné & Faherty 2018; Kounkel & Covey 2019; Torres et al. 2008; Žerjal et al. 2023), and computed the UVW velocities and XYZ space positions of those stars that have reliable astrometric data (`ruwe`<1.4) and radial velocities in the Gaia DR3 catalog. Following Gagné et al. (2021), to avoid possible contaminations, in the cases of Theia groups only member candidates separated by <5 km s^{-1} from their group characteristic velocity in the UVW space were kept. Figure 2 shows the positional $\left(\Delta_{XYZ} = \sqrt{(X-X_0)^2 + (Y-Y_0)^2 + (Z-Z_0)^2}\right)$, and velocity differences $\left(\Delta_{UVW} = \sqrt{(U-U_0)^2 + (V-V_0)^2 + (W-W_0)^2}\right)$ of these stars from J092521 whose data $(X_0, Y_0, Z_0, U_0, V_0, W_0)$ are taken from Table 2. The figure shows that both in terms of galactic space positions and velocities, members of Carina, Theia 92 and Theia 113 are the closest to J092521. Age estimates for the Carina moving group vary widely in the literature, with some recent studies leaning towards a younger age of 13 to 27 Myr (Booth et al. 2021; Kerr et al. 2022; Schneider et al. 2019; Ujjwal et al. 2020), while Bell et al. (2015) proposed an age of 45^{+11}_{-7} Myr, and the most recent

[6] https://www.exoplanetes.umontreal.ca/banyan/banyansigma.php

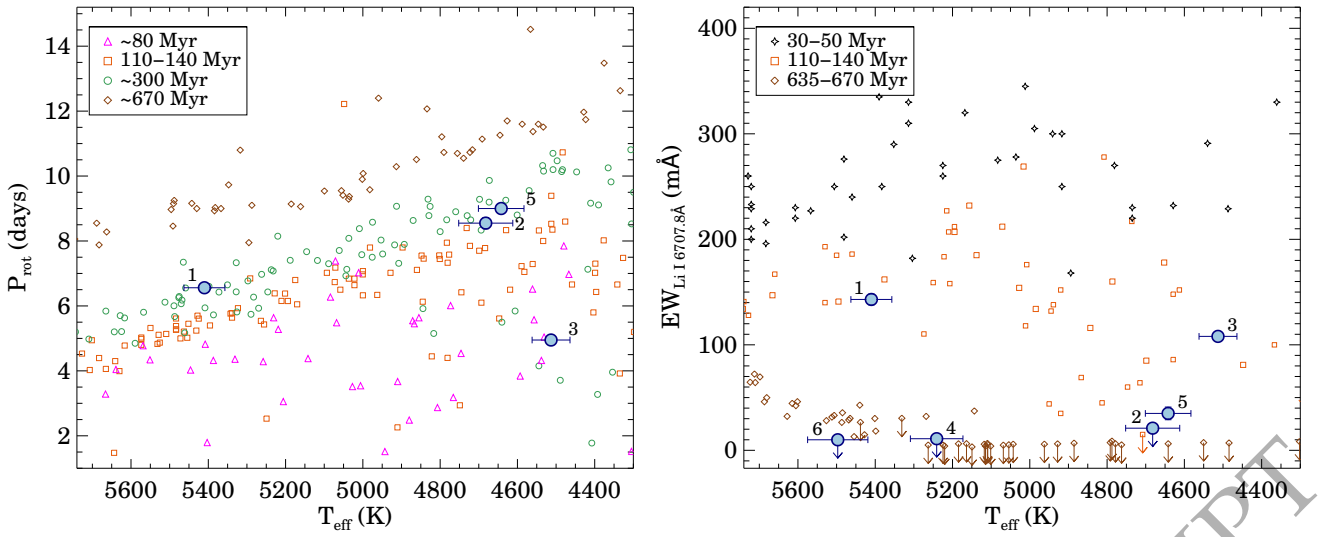

Figure 1. Left: Rotation periods as a function of effective temperatures for four of our targets (filled blue circles with error bars) and for members of seven stellar groups: α Per (~80 Myr), Blanco-1, Pleiades, Psc-Eri (110-140 Myr), NGC 3532, Group-X (~300 Myr), and Praesepe (~670 Myr). Only members that are likely to be single and have a reliable rotation period were plotted. All data were taken from Bouma et al. (2023). Right: Equivalent widths of the Li I 6708 Å as a function of effective temperature measured for our targets. For comparison Li I data of members of 8 stellar groups are also plotted: Tucana-Horologium, Carina, Columba, and Argus moving groups (30–50 Myr, da Silva et al. 2009); Blanco-1 and Pleiades open clusters (110-140 Myr, Sestito & Randich 2005; Bouvier et al. 2018), Praesepe and Hyades open clusters (635-670 Myr, Cummings et al. 2017). Our targets are marked by the following numbers in the plots: 1: J060917, 2: J071206, 3: J092521, 4: J104416, 5: J204315, 6: Gaia DR3 5366814012930376960.

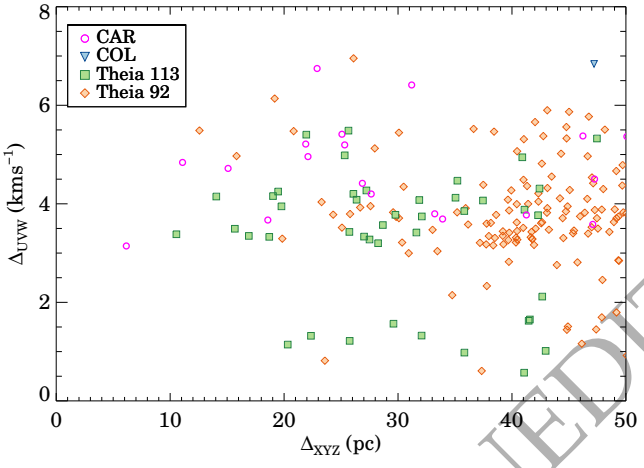

Figure 2. Velocity (Δ_{UVW}) and positional differences (Δ_{XYZ}) of members of five young stellar groups with respect to J092521. Member lists of the groups are taken from the literature: Carina (CAR) - Booth et al. (2021), Columba (COL) - Gagné et al. (2018); Gagné & Faherty (2018); Torres et al. (2008), Theia 92 and Theia 113 - Kounkel & Covey (2019). Note that in some cases the same star has been assigned to more than one group.

work based on the Lithium Depletion Boundary method yielded an age of 41^{+3}_{-5} Myr (Wood et al. 2023). For Theia 92 and Theia 113 the estimates range between 45 and 63 Myr and 45 and 71 Myr (Gagné et al. 2021; Kounkel et al. 2020), respectively. Based on the age of the groups, it is therefore more likely that J092521 belongs to Theia 92 or Theia 113 groups, but membership in the Carina cannot be completely excluded either.

J104416 forms a wide binary with Gaia DR3 5366814012930376960. We were unable to determine the rotation period for any of the components. Based on the measured upper limits of the lithium equivalent widths, the `eagles` provides age estimates of >970 Myr and >1310 Myr for J104416 and Gaia DR3 5366814012930376960, respectively. To refine this result, we performed isochrone fitting using stellar evolutionary tracks from the Dartmouth Stellar Evolution Program (DSEP, Dotter et al. 2008) and the `kiauhoku` package developed by Claytor et al. (2020). This was done for both stars, using their luminosity, effective temperature, and metallicity data as input parameters. Taking into account both age posteriors obtained as a result of these fits and the lower limit from the lithium depletion, a final posterior is calculated from which an age estimate of $5.5^{+2.4}_{-2.2}$ Gyr was obtained for the system. Because of the large total space velocity ($\sqrt{U^2+V^2+W^2} \sim 90\,\mathrm{km\ s^{-1}}$), it is a question whether J104416 might be a thick disc star. However, based on the kinematic criteria proposed by Reddy et al. (2006), it definitely belongs to the thin disc population. Using the method described in Almeida-Fernandes & Rocha-Pinto (2018) we obtained a kinematic age estimate of $7.5^{+4.3}_{-3.5}$ Gyr from the UVW data of the star. This is consistent with our result based on lithium content and isochrone fitting and adds another argument that this system is quite old.

2.7 Infrared excess and fundamental disc properties

2.7.1 Construction of the SEDs

Figure 3 displays the spectral energy distributions (SEDs) of the five systems. Most of the data at wavelengths longer than 3 μm come from measurements obtained by the *Wide-Field Infrared Survey Explorer* (*WISE*, Wright et al. 2010). During its mission, between 2010 and 2022, the *WISE* spacecraft measured our targets in 20–21 observing windows, separated by ~180 days, except for a gap between 2011 and 2013 due to hibernation of the satellite. Due to coolant depletion after 7 months, data in most windows are limited to the $W1$ and $W2$ photometric bands at 3.4 and 4.6 μm, the longer wavelength $W3$ (at 12 μm) and $W4$ (at 22 μm) observations are only available in

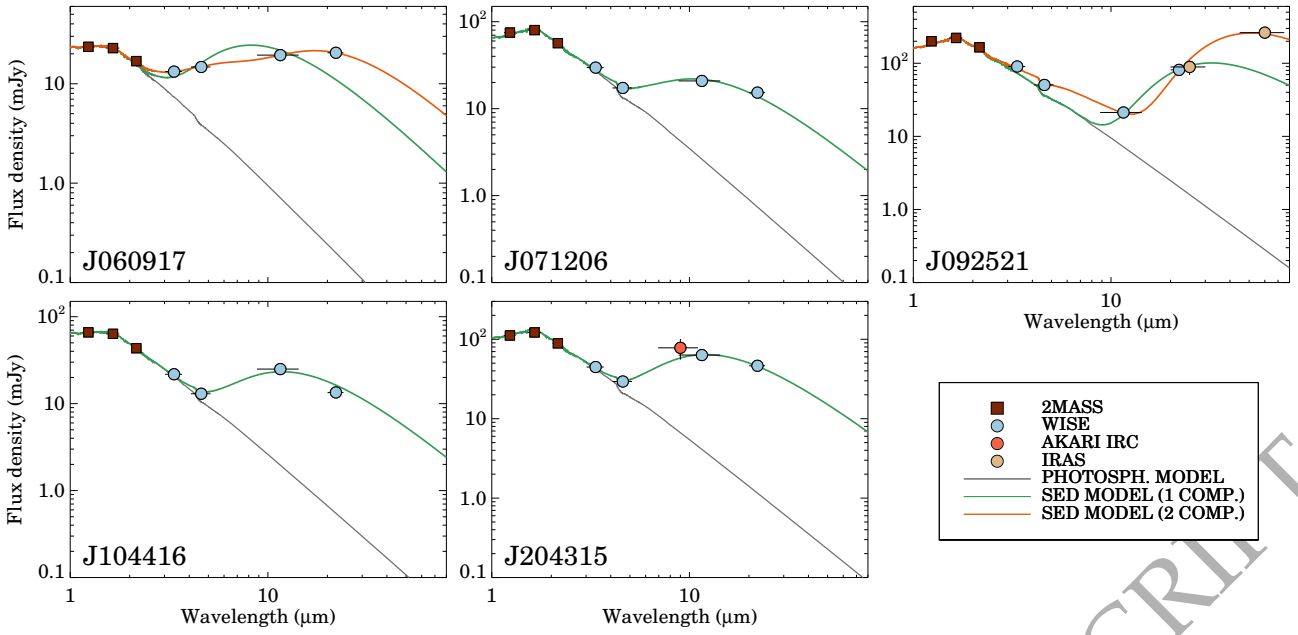

Figure 3. Spectral energy distribution of the four newly discovered EDDs and J092521 with the photosphere models and the best fit SED models. The data points shown are dereddened (using the E(B-V) estimates from Table 2) and colour corrected. Horizontal bars show the width of the filters used to take the photometric points.

the first two windows for J092521 and in the first window for the other sources. Figure 3 shows the *WISE* data obtained in the first observing window, in 2010. To derive these data, we downloaded the photometric results of the single-exposure observations from AllWISE Multiepoch Photometry tables of the NASA/IPAC Infrared Science Archive (IRSA[7]). After discarding bad quality data points, using the same strategy as in Moór et al. (2021), we computed the average of the remaining values.

We used the SCANPI[8] tool to check if any of the sources were detected in the all-sky survey performed by the *The Infrared Astronomical Satellite* (*IRAS*, Neugebauer et al. 1984). We found that J092521 was detected both at 25 and 60 μm. This source is also listed in the IRAS Faint Source Reject Catalog (Moshir et al. 1992) under the identifier of IRAS Z09244-6719. The 25 and 60 μm flux densities reported there, 78.1±17.6 mjy and 267.5±39.3 mJy, respectively, are in good agreement with the SCANPI results, so we finally used the catalogue data. Considering the proper motion of J092521, taken from the Gaia DR3 catalogue, the star is located 8.″4 from the IR source, within the error ellipse. The *WISE* W4-band image shows that there are no other bright sources in the vicinity of J092521; this together with the fact that the *WISE* 22 μm and the *IRAS* 25 μm fluxes are in good agreement (see Fig. 3), indicates that the *IRAS* detections are also likely associated with J092521. Looking through the *AKARI* IRC (Ishihara et al. 2010) all-sky infrared catalogues, we found that J204315 was measured at 9 μm.

2.7.2 *Modelling of the infrared excess*

Fig. 3 shows that all five objects exhibit strong IR excess implying the presence of warm circumstellar dust. Previous measurements of EDDs have shown that they tend to display substantial variability at

Table 5. VISIR observations

Name	Obs. date	Band	Flux density (mJy)
TYC 5940	2022-01-29	B8.7	38.3±2.1
	2022-01-29	B10.7	98.6±5.0
	2022-01-29	B12.4	30.0±2.5
J060917	2022-01-30	B8.7	20.3±1.3
	2022-01-30	B10.7	28.6±1.6
	2022-01-04	B12.4	20.5±1.5
TYC 8105	2022-01-30	B8.7	57.1±3.0
	2022-01-30	B10.7	89.8±4.6
	2022-01-30	B12.4	64.7±3.8
J071206	2022-01-30	B8.7	14.7±1.0
	2022-01-30	B10.7	46.6±2.5
	2022-01-30	B12.4	15.0±1.4
J092521	2022-01-29	B8.7	25.8±1.6
	2022-01-29	B10.7	24.4±1.6
	2022-01-05	B12.4	14.1±1.4
J104416	2022-01-31	B8.7	21.6±1.4
	2022-01-31	B10.7	45.6±2.5
	2022-02-10	B12.4	18.3±1.5
TYC 4946	2022-01-31	B8.7	31.2±1.8
	2022-01-31	B10.7	28.7±1.7
	2022-02-14	B12.4	15.3±1.3
J204315	2022-05-31	B8.7	57.6±3.1
	2022-05-31	B10.7	104.5±5.4
	2022-05-31	B12.4	38.5±3.1

[7] https://irsa.ipac.caltech.edu/applications/wise/
[8] https://irsa.ipac.caltech.edu/applications/Scanpi/

least at 3–5 μm (Su et al. 2019; Moór et al. 2021, 2022; Rieke et al. 2021). Therefore, initally only the simultaneously measured *WISE* data points were used to characterize the excess that are fitted by a single temperature blackbody model. In the fitting we employed Levenberg-Marquardt algorithm using the IDL code developed by Markwardt (2009) to estimate the characteristic dust temperature and the solid angle of the disc as free parameters. Utilizing the results of an initial fit we performed the colour correction of the data points, and then we used the corrected data in the final fitting (for more details see, Moór et al. 2021). This simple model provides good results for J071206, J104416, and J204315 (Fig. 3), yielding dust temperatures ($T_{\rm d}$) of 434±25 K, 405±21 K, and 404±15 K and fractional luminosities ($f_{\rm d} = L_{\rm disc}/L_*$) of 0.026, 0.025, and 0.048, respectively. On the other hand, poor quality of the fits for J060917 and J092521 suggested multiple temperature dust components in these systems. As Figure 3 demonstrates, by adopting a two-temperature model and including the 2MASS data in the fit, we have achieved a much more convincing result for J060917, where hot and warm dust components have temperatures of 752±48 K and 237±22 K, and fractional luminosities of 0.075 and 0.027. In line with this, a comparison between the values of the corrected Akaike Information Criteria ($\rm AIC_c$, Burnham & Anderson 2002) calculated for the one- and two-component models confirmed the better quality of the latter approach. The total fractional luminosity of this disc is thus ~0.1, which is remarkably high even among EDDs (see Figure 6). For J092521, Higashio et al. (2022) has already proposed a two-temperature disc model based on *WISE* data only. If the *IRAS* data points are also included in the fit, the necessity of a second colder dust component is even more striking, and this is also confirmed by our comparison based on $\rm AIC_c$. Using such a model, we obtained $T_{\rm d,warm} = 857\pm90$ K and $f_{\rm d,warm} = 0.021$ for the warm and $T_{\rm d,cold} = 99 \pm 6$ K and $f_{\rm d,cold} = 0.033$ for the cold dust. *WISE* photometry in all 4 bands are available for this source in a second epoch, half a year after the first. Repeating of the fitting process using this second data set, resulted in the following disc parameters: $T_{\rm d,warm} = 859\pm69$ K, $f_{\rm d,warm} = 0.031$, $T_{\rm d,cold} = 97\pm6$ K, $f_{\rm d,cold} = 0.032$. Our results in both epochs are broadly consistent with the ones obtained by Higashio et al. (2022) ($T_{\rm d,warm} = 1108^{+278}_{-393}$ K, $f_{\rm d,warm} = 0.021$, $T_{\rm d,cold} = 150^{+37}_{-13}$ K, $f_{\rm d,cold} = 0.016$).

Assuming the presence of blackbody particles, the $R_{\rm BB}({\rm au}) = (278.3/T_{\rm d}(K))^2 L_*(L_\odot)^{0.5}$ formula (Wyatt 2008) gives an estimate of the distance of the emitting warm dust from the star. For J071206, where the presence of a nearby companion is very likely, we have assumed that the disc surrounds the primary component. The luminosity of the star was estimated from its effective temperature by intepolation in the table of basic parameters for dwarf stars compiled by Pecaut & Mamajek (2013). For J061709 and J092521, the excess can be described by two temperature components. In the calculation of $R_{\rm BB}$, it was assumed that this indicates the presence of two distinct dust rings, which is, however, not necessarily the case. The warm rings in these systems have $R_{\rm BB}$ between 0.05–0.3 au, while in two systems there are also colder dust material at 1–3.7 au.

The obtained disc parameters are summarized in Table 2.

2.7.3 *Infrared variability*

To assess whether any of the four newly discovered EDDs or J092521 exhibited significant variability at 3.4 and/or 4.6 μm between 2013 and 2022, we analysed their single-exposure $W1$ and $W2$ band photometric measurements downloaded from NEOWISE-R Single Exposure Source Table archived by IRSA. After we removed data points of dubious quality using the flags assigned to the measurements and following the method proposed by Moór et al. (2021), we computed the $\chi^2_{\rm red}$ tests for each band individually and the Stetson J (S_J) index that measures correlated variability in the $W1$ and $W2$ bands (Sokolovsky et al. 2017). To determine whether the discriminants obtained in this way indicate significant changes, it is necessary to define a threshold, which is derived in each case by comparison with the ensemble of variability indices calculated for *WISE* sources of similar brightness ($\Delta W_1 = \pm1$ mag, $\Delta W_2 = \pm1$ mag) located within 1°.5 of the target. After identifying and removing outliers using a sigma clipping procedure, the means ($D_{\chi^2_{\rm red,W1}}$, $D_{\chi^2_{\rm red,W2}}$, D_{S_J}) and the standard deviations ($\sigma D_{\chi^2_{\rm red,W1}}$, $\sigma D_{\chi^2_{\rm red,W2}}$, σD_{S_J}) were calculated for the comparison sample, and the threshold was calculated as $D_x + 5\sigma D_x$ (see also in Moór et al. 2021).

We concluded that all of our targets are variable. J060917 and J092521 show significant and correlated changes in both bands, while for the other three objects the variability is limited to the $W2$ band. In the $W1$ and $W2$ bands both the star and the circumstellar disc contribute to the observed emission. With the exception of J060917, where the contribution of the disc is ~48% and ~76% of the total flux density at 3.4 and 4.6 μm, respectively, for the other objects the stellar photosphere dominates the emission in both bands. It is therefore worth scrutinizing whether possible changes of the host stars could explain the variability observed in the *WISE* light curves. By examining the available ASAS-SN light curves, we found that the brightness of the targets was stable over the given timescale and did not show any similar pattern to the changes seen in the *WISE* data streams. That the observed variations are related to the discs is also supported by the fact that their amplitudes, in correlation with the larger contribution of the disc to the total flux, are always larger in the W2 than in the W1 band (or can only be detected in the W2 band).

By averaging the individual single exposure data points in each *WISE* observing window between 2013 and 2022, and by subtracting the stellar contribution from the measured flux densities using the photosphere models (Sect. 2.4), we compiled and plotted the $W1$ and $W2$ light curves of the five discs that are found to be variable (Fig. B1).

3 VLT/VISIR OBSERVATIONS

In order to assess whether the 8 targeted EDDs display N-band solid state features, we used the VLT Imager and Spectrometer for the mid-InfraRed (VISIR, Lagage et al. 2004) on ESO's Very Large Telescope (VLT, UT2) to measure their flux densities in three bands at 8.91 μm (B8.7), 10.64 μm (B10.7), and 12.45 μm (B12.4). The observations were carried out under ESO programme 106.212F.001 (PI: A. Moór). We used the regular imaging mode with the Small Field objective that provides a field of view of 38″×38″with a pixel scale of 45 mas×45 mas[9]. To subtract the sky background, chopping and nodding was used with a chop throw of 8″ perpendicular to the nodding direction. While for the brightest sources all three band measurements were taken at the same time in the same run, fainter objects were observed in two separate runs (see Table 5). Using the same filters, immediately before or after our main targets' measurements, we also observed a nearby mid-IR standard star that was selected from the catalogue compiled by Cohen et al. (1999). The average airmass

[9] https://www.eso.org/sci/facilities/paranal/instruments/visir/doc/VLT-MAN-ESO-14300-3514_2020-03-03.pdf

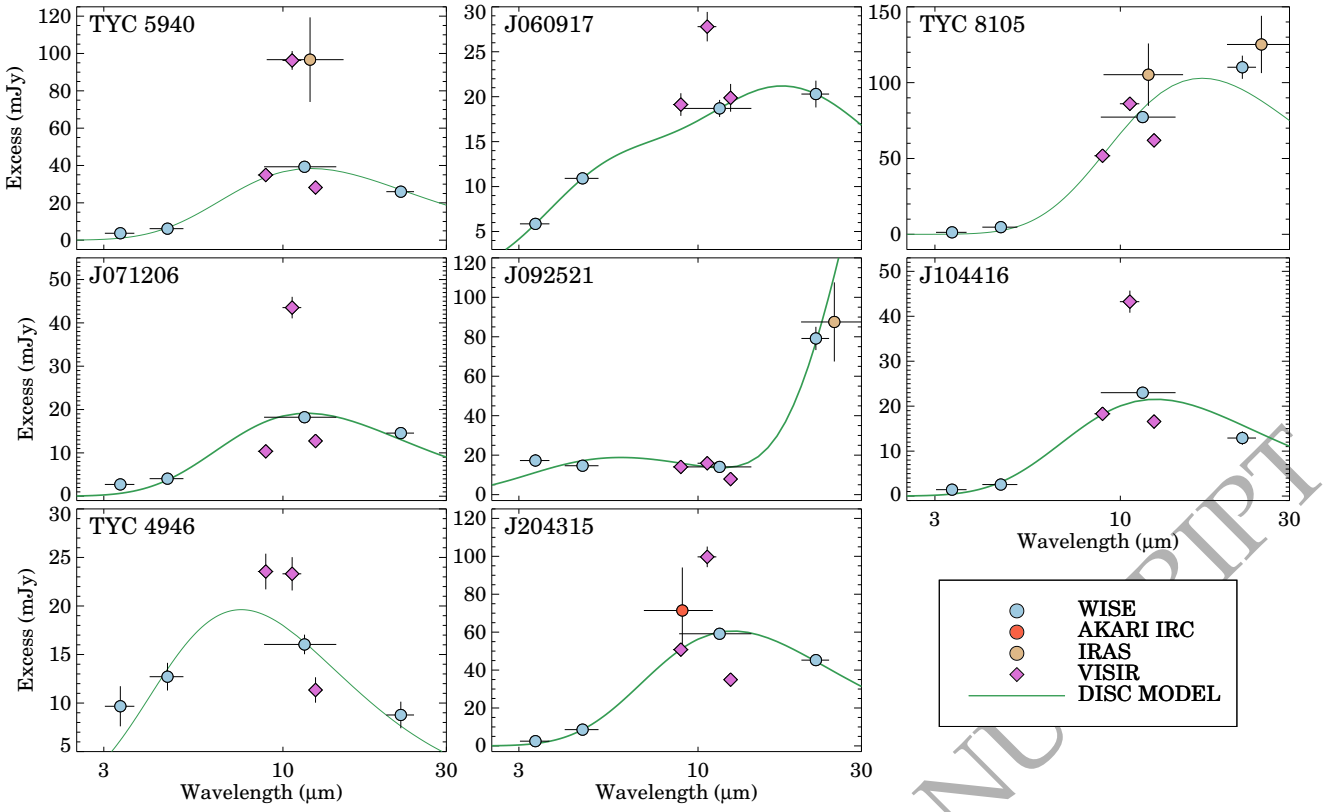

Figure 4. Spectral energy distribution of the excess emission. Our new VISIR data points are marked by violet diamonds, while the symbols for *IRAS, WISE* and *AKARI* observations are the same as in Fig. 3. Horizontal bars show the width of the filter used. The disc models, that are taken from Sect. 2.7.2 and from Moór et al. (2021), are indicated by green lines.

difference between the target and the corresponding standard object was 0.03, with a maximum difference of 0.15.

We used the EsoReflex GUI environment (Freudling et al. 2013) with VISIR 4.4.2 pipeline kit[10] and the `visir_img.xml` workflow to reduce and calibrate our raw data sets. The pipeline produced a flux calibrated image as well as an uncertainty image. All our targets in all bands have been detected as single point sources in the images. In most cases the objects have circularly symmetric brightness profile, the only exception is J204315, which due to its position in the sky, has been measured at relatively large zenith distances and therefore it has an elongated shape especially at 8.91 and 10.64 μm. The average full width at half-maximum of the sources is ~6, ~7, and ~8 pixels (272, 317, and 362 mas) in 8.91, 10.64, and 12.45 μm. To extract their flux densities we applied aperture photometry with a radius of 6 pixels (10 pixels for J204315) in all bands. The background was estimated in an annulus between 20 and 30 pixels. To determine the internal photometric error we used the uncertainty image produced by the pipeline. The aperture correction factor for a given observation was derived using the associated standard star measurement. By comparing the flux densities obtained for our standard stars with the expected values taken from the literature (Cohen et al. 1999, and the table available on the VISIR homepage[11]), we found that they reproduce them with an ~5% average accuracy. We therefore calculated the final photometric uncertainty as the quadratic sum of the internal measurement error and this calibration uncertainty. The obtained flux densities and their uncertainties are listed in Table 5.

4 RESULTS

In Figure 4 we present the SEDs of the excess emission for all 8 targets. In addition to the available broad-band photometry, the narrow-band VISIR data are also plotted (the horizontal bars show the width of the used photometric bands[12]. For TYC 5940, TYC 8105, and TYC 1213, mid-IR data other than the VISIR photometry and the photospheric models used to compute the excesses are taken from Moór et al. (2021). As can be seen, VISIR data points typically peak in the B10.7 band and show abrupt changes in the narrow spectral region examined, indicating the presence of solid state features in the SED.

To investigate this further, we compared our results with the outcomes of mid-IR spectroscopic studies carried out by *Spitzer* for nine warm debris discs showing prominent solid-state features (Fig. 5, top). Seven objects (BD+20 307, P 1121, ID 8, HD 113766, HD 15407, HD 23514, and HD 145263) from the selected sample are classified as EDDs in the literature. Although the fractional luminosity of the other two discs, around HD 69830 and HD 172555, is substantially lower (2.4×10^{-4} and 7.2×10^{-4}, respectively, Mittal et al.

[10] https://ftp.eso.org/pub/dfs/pipelines/instruments/visir/visir-reflex-tutorial-1.5.pdf

[11] https://www.eso.org/sci/facilities/paranal/instruments/visir/tools.html

[12] The effective widths of the filters are taken from the SVO filter profile service (http://svo2.cab.inta-csic.es/theory/fps/).

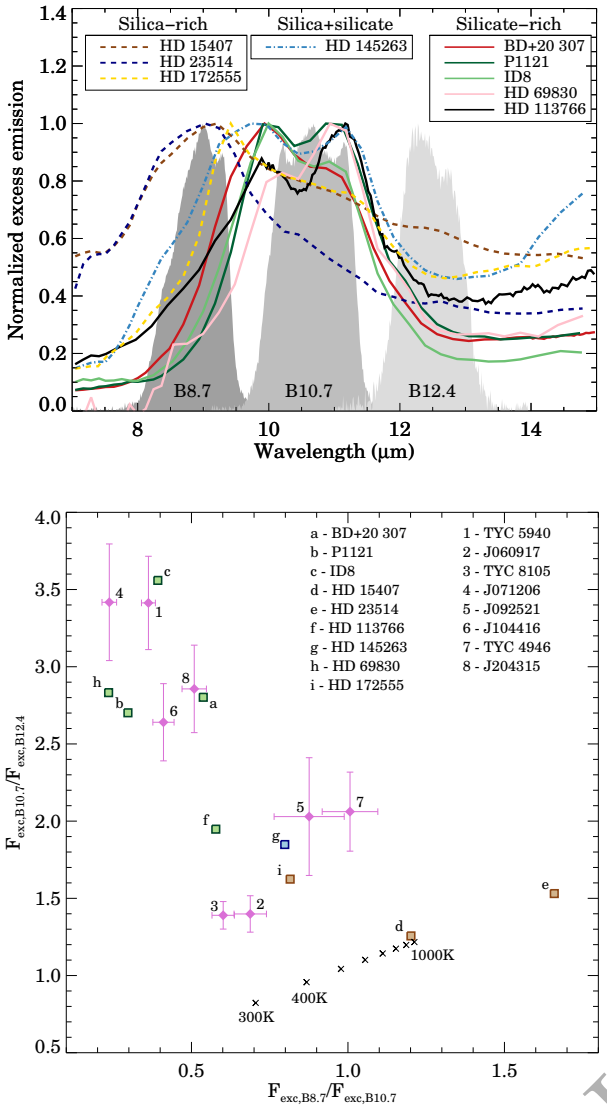

Figure 5. Top: Normalized excess spectra between 7 and 15 μm of nine debris discs with transient origin. The original *Spitzer* spectra, from which they were derived, were taken from the literature (Chen et al. 2006; Lebouteiller et al. 2011; Su et al. 2020, see Sect. 4 for more details). Transmission curves of the three applied band-pass filters (B8.7, B10.7, B12.4) are also displayed. Bottom: $F_{\rm exc,B10.7}/F_{\rm exc,B12.4}$ flux ratios as a function of $F_{\rm exc,B8.7}/F_{\rm exc,B10.7}$ ratios for our eight targets (purple diamonds) and for the nine abovementioned discs (squares) with high quality mid-IR spectra obtained with the *Spitzer*/IRS spectrograph. For the latter objects, synthetic photometry was used to derive the flux ratios, the silicate- and silica-dominated discs are marked in green and brown, respectively, while HD 145263 is marked in blue.

2015) than that of EDDs, their warm dust material is thought to have transient origin (Beichman et al. 2005; Wyatt et al. 2007; Lisse et al. 2009; Johnson et al. 2012).

Looking at the spectral range we have examined, between 8 and 13 μm, two groups can be broadly distinguished on the basis of the observed solid state features (Sect. 1). Five of these discs (BD+20 307, P 1121, ID 8, HD 113766, and HD 69830) have strong solid-state emission features between 10 and 11.5 μm, implying the presence of fine amorphous and crystalline silicate dust particles (Olofsson et al. 2012; Morlok et al. 2014; Meng et al. 2015). The spectra of HD 15407 and HD 23514 peak at ~9 μm, indicative of copious amount of small silica grains (Rhee et al. 2008; Olofsson et al. 2012; Morlok et al. 2014; Meng et al. 2015). The disc around HD 172555 is also rich in silica as evidenced by a dominant feature at ~9.3 μm (Lisse et al. 2009). The HD 145263 represents a kind of transition between the two groups with its mid-IR spectrum indicate the presence of some silica in the disc in addition to silicates (Lisse et al. 2020). For comparison with our data, we had to extract synthetic photometry from the available low-resolution IRS spectra. With the exception of HD 113766 and HD 172555, the spectra were retrieved from the LR7 release of the Cornell AtlaS of Spitzer/IRS Sources (CASSIS; Lebouteiller et al. 2011) database, which provides uniformly processed, high-quality IRS spectra. Being spatially unresolved, for all seven sources we selected the data product obtained using the optimal extraction. HD 145623 was observed three times with the IRS. Since these measurements show no variability around 10 μm, we finally chose the middle observation (AOR: 21808896) for our analysis. HD 69830, which was the subject of a multi-epoch mid-IR spectroscopic monitoring project carried out by the *Spitzer* (Beichman et al. 2011), has 6 low-resolution IRS spectra in the CASSIS database, from which we used the one with the AORkey of 28830720. In the case of HD 113766 and HD 172555, where the IRS observations were performed in spectral mapping mode, and thus is not included in CASSIS, the spectra were taken from the literature (Chen et al. 2006; Su et al. 2020). From these spectra then we computed synthetic photometry in the three VISIR bands using the relevant filter profiles downloaded from the VISIR homepage[13]. To calculate excesses we also needed the stars' photospheric models, that were taken from Moór et al. (2021). IRS spectra between 7 and 15 μm of the nine discs as well as the three filter profiles are displayed in the top panel of Fig. 5.

Figure 5 (bottom) shows the flux ratios of $F_{\rm exc,B10.7}/F_{\rm exc,B12.4}$ as a function of $F_{\rm exc,B8.7}/F_{\rm exc,B10.7}$ ratios for our targets (violet diamonds) and for the selected nine discs observed by the *Spitzer* (squares, green for silicate-dominated discs, brown for systems with silica features, and blue for HD 145263). The measured flux ratios of our targets (violet diamonds) are substantially different from those of plain blackbodies with temperatures between 300–1000 K (black crosses). TYC 5940, J071206, J104416, and J204315 coincide well with four silicate-dominated discs (BD+20 307, P 1121, ID 8, and HD 69830), indicating that their solid state emission features may be broadly similar to those detected in the spectra of the latter objects. The $F_{\rm exc,B8.7}/F_{\rm exc,B10.7}$ flux ratios of the other four discs are higher. They occupy roughly a region in the figure where both silicate-rich and silica-rich discs from the *Spitzer* sample are found, and thus they cannot be classified with certainty on the basis of our current data. In the case of J092521 and TYC 4946, the $F_{\rm exc,B8.7}/F_{\rm exc,B10.7}$ flux ratios exceed that measured for HD 145263, but is below that of HD 15407 and especially HD 23514. This, and the proximity of the two objects to HD 145263 in the figure raises the possibility that these discs also contain some silica grains. However, their difference from HD 23514 suggests that silica, if present at all in them, may be much less dominant than in the latter EDD.

Based on our measurements, thus, the majority of the sources studied may show strong solid state features around at least 10 μm. Because of this, the true shape of the SED may even differ substantially from the blackbody model fitted to the broadband photometric

[13] https://www.eso.org/sci/facilities/paranal/instruments/visir/inst.html

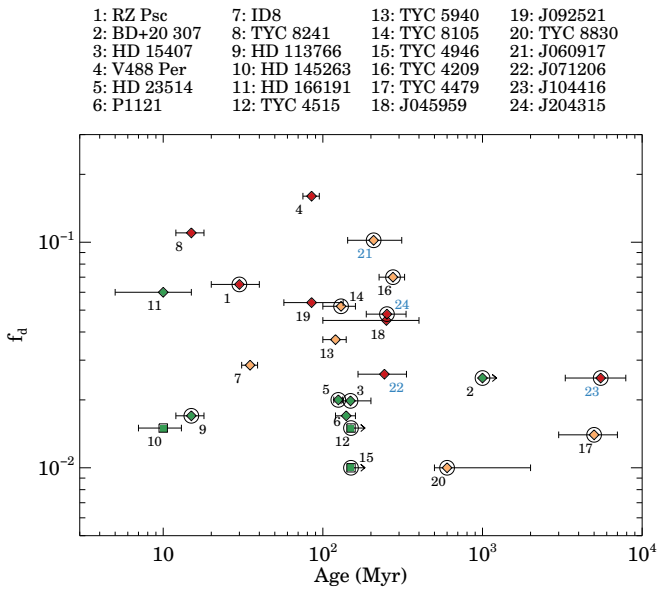

Figure 6. Fractional luminosity as a function of age for 20 EDDs from the literature (marked by black numbers) and for our four new discoveries (marked by blue numbers). Spectral type of the host stars are indicated by colours (F-type: green, G-type: light orange, K-type:red). Objects with significant changes at 3–5 μm are marked with diamond symbols while non-variables are marked with squares. Multiple systems are indicated by larger circles around the symbols. Due to their variability, the f_d of the discs is likely to vary, but the extent of this is difficult to estimate, as our time-domain data are mostly limited to a narrow wavelength interval between 3 and 5 μm range. The TYC 8241 disc has depleted significantly after 2010 (Melis et al. 2012), the data point shown corresponds to the pre-2010 state. Some of the object identifiers above the figure are abbreviated, therefore in Table C1 we provide the corresponding AllWISE identifiers of all systems and, where available, their SIMBAD-compatible names.

data, and thus the true dust temperatures may show deviations from the fitted values that could be even significantly larger than the formal errors derived in Sect. 2.7.2.

5 DISCUSSION

5.1 Age distribution and age related trends of EDDs

The four new discoveries presented here together with the 20 discs known from the literature (including the other four objects we analyze in the paper) raises the total number of known EDDs around F-K-type main-sequence stars to 24 (see Table C1). In the following, we review their basic characteristics, their dependence on age, and examine the age distribution itself.

Figure 6 shows the fractional luminosity of EDDs as a function of age. The data for this plot were taken from Table 2 and from the literature (Vican et al. 2016; Tajiri et al. 2020; Melis et al. 2021; Moór et al. 2021, and references therein). EDDs are typically defined as objects with $f_d \gtrsim 0.01$, and thus they represent the highest fractional luminosity tail of the transient debris disc population. An observable feature of the distribution is that the f_d of discs hosted by F-type stars (indicated by green symbols) tend to be smaller than those around G- (light orange) and K-type (red) stars. This does not necessarily mean there is less dust in EDDs around the F-type stars. This trend may be partly related to the stronger radiation pressure of the more luminous F stars, which can thus blow out much larger grains than in the case of G, K stars, thereby resulting in a smaller f_d for the same dust composition, mass and radial distance. Another explanation could be that the average radial distance of the EDDs around F-type stars is larger than around later spectral type hosts. The available R_{BB} data hint at such a trend, but as the uncertainty may be particularly high for systems with sparsely sampled SEDs, no firm conclusions can be drawn at present. The high fractional luminosity of the EDDs and the complex mid-infrared light curves they exhibit suggest that there are regions in the discs that are optically thick (Kennedy et al. 2014; Meng et al. 2014; Su et al. 2019) at least at wavelengths shorter than a few microns, which may further complicates this issue. Another notable trend in Figure 6 is that the majority of discs around G- and K-type stars younger than 300 Myr have $f_d > 0.03$, while older EDDs with similar host stars (although very few are known) exhibit f_d lower less than this value.

Thanks to the NEOWISE reactivation mission, light curves with a cadence of a half year at 3.4 and 4.6 μm are available for all EDDs, allowing the investigation of possible annual variations in the last decade. In addition, some EDDs were also monitored with *Spitzer* at 3.6 and 4.5 μm (e.g. Meng et al. 2014; Su et al. 2019, 2020, 2022). By studying the 17 EDDs known at that time, Moór et al. (2021) found that 14 of them show significant variability in the 3–5 μm range, i.e. this is an inherent property of EDDs. The observed rapid changes of EDDs are mostly attributed to the dynamical and collisional evolution of a cloud of fresh dust produced after vaporisation and subsequent condensation of material ejected in a high velocity impact (Jackson et al. 2014; Su et al. 2019, 2022; Watt et al. 2021; Moór et al. 2022; Lewis et al. 2023). The NEOWISE light curves of five of the seven objects discovered since then have been analysed in Sect. 2.7.3. For the other two EDDs, TIC 43488669 (J045959; Tajiri et al. 2020) and TYC 8830-410-1 (TYC 8830; Melis et al. 2021), proceeding in a similar spirit, we found that both discs are variable (see Fig. B1 for light curves of the discs). In Figure 6, variable objects – the majority of the sample, 21 systems out of the 24 – are marked by diamonds, while those displaying no significant changes are shown by squares. This statistic further reinforces the abovementioned finding that mid-IR variability is a fundamental characteristic of EDDs.

Current theories mostly link the formation of EDDs to giant collisions taking place in the region of terrestrial planets (Melis 2016; Su et al. 2019). Such collisions between large planetary embryos are thought to be common during the final chaotic growth phase of rocky planets, raising the possibility that EDDs may indeed be the result of these events. However, according to simulations, these planet-forming processes occur mostly in the first tens of million years, and the frequency of collisions drops off significantly after 100 Myr (e.g. Quintana et al. 2016). Consistent with this picture, recent studies suggest that the era of giant impacts in the Solar System probably ended by 80 Myr (Woo et al. 2022). Looking at the age distribution of the currently known EDDs (Fig. 6), we see that their incidence tends to decrease very slowly in the first 300 Myr: there are 8 objects younger than 100 Myr, 7 with ages between 100 and 200 Myr (5 if we assume that the two objects with only a lower age limit of 150 Myr are indeed much older), and 5 between 200 and 300 Myr. Considering not only perfect accretion but fragmentation and hit-and-run collisions in their simulations of rocky planet formation around Sun-like stars, Quintana et al. (2016) found (see their fig. 5) that ~95% of the large collisions happen in the first 100 Myr and ~4% between 100 and 200 Myr. This is very different from what we see in the observed sample, and suggests that the formation of EDDs is not exclusively related to the formation of rocky planets, but other mechanisms, some

of which are activated later, may also play an important role. Hansen (2023) raises the possibility that the tidal evolution of a planet-moon system can lead to the escaping of the moon, which then can collide with its original parent planet. Such process could result in collisions on a similar scale to those that are thought to occur during formation of the rocky planets, but at a much later time, thereby explaining the existence of older EDDs. Another alternative explanation is that the increased dust production may be linked to some sort of rearrangement of the planetary system. This can also occur in young systems, for example, the dusty disc of RZ Psc is proposed to be related to the migration of recently formed giant planets, that might be initiated by the known companion (see below) of the star (Su et al. 2023). In an older system, a late dynamical instability can trigger processes that cause significant episodic dust production in the terrestrial zone via large collisions, and/or sublimation of a swarm of icy bodies transported into that region from an outer reservoir (e.g., Melis et al. 2021; Moór et al. 2021).

Previous studies suggested that wide-separation companion stars may play a role in the formation of warm dust-rich discs (Zuckerman 2015; Silverberg et al. 2018; Moór et al. 2021). In Figure 6, known multiple systems are indicated by larger circles around the symbols. For TYC 5940, J092521, and in particular J071206, the Gaia DR3 radial velocity or astrometric data strongly suggest the presence of companion stars (Sect. 2.3), but these are not yet considered secure results and are therefore not marked in the figure. Two of the eight EDD host stars younger than 100 Myr are known to be binaries, RZ Psc has a companion at a projected separation of ~20 au (Kennedy et al. 2020), while the projected separation between the two components of the HD 113766 system, based on their Gaia DR3 data, is ~150 au. At least 75% (12/16) of objects older than 100 Myr have a companion, their projected separations range between 365 and 10261 au[14]. In this older subgroup, thus, the fraction of binaries with separation >300 au is significantly higher than among the younger EDDs. This incidence of wide binary pairs is also significantly higher than that observed for normal main sequence stars with similar spectral type (Moór et al. 2021). Remarkably, all EDD host stars older than 500 Myr have known wide companions.

This observed characteristic of older EDDs suggests that their wide companions might have played a role in the formation of the disc, for example by triggering a late dynamic instability in their planetary systems. Although the companions are currently very far away from the discs, wide binary systems, in particular the equal-mass pairs, tend to have highly eccentric orbit (Tokovinin & Briceño 2020; Hwang et al. 2022a,b), i.e. it is possible that the processes that led to the disc's formation were triggered during the last pericentre passage of the pair. A recent catalogue compiled by Hwang et al. (2022a) using Gaia astrometry, contains estimates of the eccentricities of 10 binary EDD systems. Figure 7 shows the most probable eccentricities and the lower and upper eccentricity limits of the 68% credible interval for those 8 object, where all quality criteria proposed by Hwang et al. (2022a) (in Sect. 4.3 of their work) are fulfilled. For the three oldest EDDs with ages $\gtrsim$1 Gyr (BD+20 307, TYC 4479, J104416) and for TYC 4946, which has only a lower age estimate of 150 Myr, the best eccentricity estimate is 0.99, with a confidence interval upper bound of 1 and lower bounds of ~0.75. With such large eccentricities, even with the relatively large projected separations of 10^3–10^4 au measured for these systems, it is plausible to assume that the (probably most recent) pericentric passage of the companion could have significantly perturbed the possible planetary systems. Thus, these objects could be promising candidates that are just now undergoing a dynamic instability process, e.g. akin to the hypothesized Late Heavy Bombardment in the Solar system.

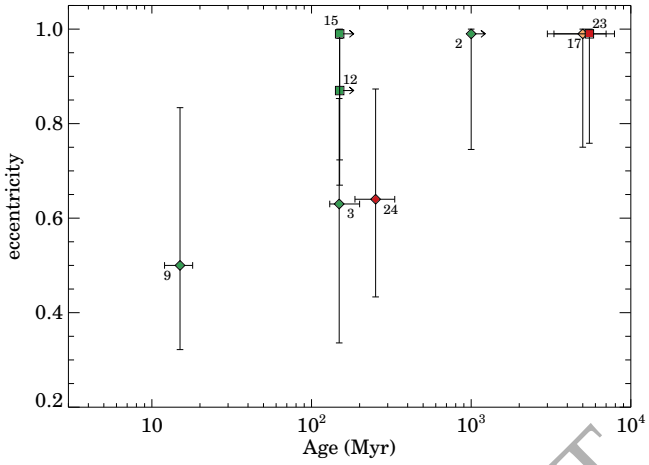

Figure 7. Estimates of eccentricities of 10 binary EDD systems based on Hwang et al. (2022a). The vertical error bars correspond to the lower and upper eccentricity limits of the 68% credible interval. See Fig. 6 to identify which objects the numbers represent.

The orbital plane of the companion star may also be different from that of the planetary system including the planetesimal disc(s). In case of sufficiently high mutual inclination, the companion can affect the orbit of the smaller bodies via the Kozai-Lidov mechanism, leading to oscillation in their eccentricity and inclination (Naoz 2016). This could cause stronger excitation of the disc, more frequent collisions and hence enhanced dust production (Nesvold et al. 2016; Moore et al. 2023), or even drive icy planets in the outer belt into the inner regions by increasing their eccentricity, where they can contribute to the dust disc via their sublimation and disruption (e.g. Young & Wyatt 2023). Whether these mechanisms can indeed explain the very high dust content of EDDs require further investigations.

5.2 Solid-state feature from sub-micron grains

In addition to the *Spitzer* IRS observations mentioned in Sect. 4, ground-based mid-IR spectroscopic observations around 10 μm are available for four EDDs: RZ Psc (Kennedy et al. 2017), V488 Per (Sankar et al. 2021), HD 166191 (Kennedy et al. 2014), and TYC 8830-410-1 (Melis et al. 2021). Of these, only V488 Per shows no detectable solid-state emission, the other three display clear solid-state features peaking between 10 and 11 μm indicating the presence of small amorphous and crystalline silicates in their discs (Kennedy et al. 2014, 2017; Melis et al. 2021). By taking into account the outcome of our multiband photometric programme as well, now we have information on solid-state emission around 10 μm for 19 of the 24 EDDs identified so far. Even in this larger sample, V488 Per is the only one that is probably featureless. For the vast majority of EDDs' mid-IR spectra, the most dominant solid-state features present between 10 and 11.5 μm, indicating silicate-rich dust material, with only two systems (HD 15407, HD 23514) so far known where the spectra are dominantly characterised by features

[14] BD+20 307 is a triple system consisting of a close inner binary (Weinberger 2008; Zuckerman et al. 2008) and a distant tertiary component with a projected separation of ~980 au, as recently revealed using Gaia DR2 astrometric data (Moór et al. 2021).

between 9 and 9.5 μm as an indication of significant amount of silica grains. In addition to them, HD 145263 exhibits both silica and silicate emission features (Lisse et al. 2020) and based on our VISIR multiband observations we have identified two other EDDs, J092521 and TYC 4946 that may have a similar characteristic. By comparing mid-IR *Spitzer* spectra of warm debris discs with the spectra of solar system rocky samples, Morlok et al. (2014) argued that the material of silicate-dominated discs are more mantle-type while the silica-bearing objects are associated with crustal-type materials.

An interesting question is whether the above groups based on solid-state emission features show any correlation with the mid-IR time-domain behaviour of the objects (see also in Meng et al. 2015). The level of the variability can be characterised in many ways. In the following we generally use the χ^2 statistic of the *W*2 NEOWISE Reactivation light curves of the sources as a metric for this purpose. Among the silica-bearing EDDs, the *WISE* light curves of HD 15407 show no variability, although due to its high brightness the measurements are saturated which degrades the quality. However, based on its *Spitzer* time-domain data, a weak but significant variability was detected (Meng et al. 2015). HD 23514 shows moderate flux level changes, while for HD 145263 neither its *WISE* nor its *Spitzer* data show significant variations. Out of the two newly identified silica-bearing candidates, TYC 4946 is also non-variable, while J092521 is one of the five most highly variable objects (along with RZ Psc, ID 8, V488 Per, and TYC 4209). Overall, it seems that the mid-IR variability level of the objects and candidates belonging to this group seems to be rather low. The light curves of the silicate-rich EDDs – here we include those four objects from the VISIR mini-survey for which there is a strong indication to have this property (TYC 5940, J071206, J104416, and J204315, see Sect. 4) – all show variations, and ID8 and RZ Psc are among the objects that have particularly high variability. The average level of variability in this group is higher than for silica-bearing discs (see also in Meng et al. 2015). Finally, V488 Per, with the most extreme amplitude and very rapid changes, was found by Sankar et al. (2021) to be featureless based on its 8–13 μm spectrum. Considering this result they suggest the presence of dust composed primarily of metallic iron in this disc.

Silica grains are thought to be produced via condensation from silica-rich vapor formed in high-velocity (5–10 km s^{-1}) giant impacts (e.g., Lisse et al. 2009, 2012) or in hypervelocity ($\gtrsim$ 10 km s^{-1}) collisions between sub-millimeter-sized particles (Johnson et al. 2012). Based on these hypotheses one would expect some correlation between the presence of silica and variability, since the latter phenomenon is also interpreted as an aftermath of high-velocity collisions (Meng et al. 2015; Su et al. 2019). Contrary to this expectation, however, silica-bearing discs typically show only weak mid-IR changes. A possible explanation for this is that silica particles can also be formed in other ways. Lisse et al. (2020) argued that in the disc of HD 145263, space weathering triggered by a stellar superflare altered the original dust material leading to the appearance of such particles. However, for the silica material of HD 23514 and HD 15407, they also favour a collisional origin. For the latter discs, the IRS observations were performed in 2008, while most *Spitzer* or *WISE* photometric data at 3–5 μm were obtained after 2010. Models of post-impact processes suggest that the most pronounced brightness changes in the resulting debris disc occur within a few orbital periods after the impact, which for most EDDs takes a few years at most. If the collisional evolution and grinding of the resulting silica dust population takes longer than this, then it is possible that the impact event and the most substantial brightness changes already took place well before the spectroscopic observations, in a period when no monitoring data were available.

6 SUMMARY

Extreme debris discs are peculiarly bright warm circumstellar dust structures around some main sequence stars. They have transient origin and likely represent the outcome of a giant collisional event that happened within the terrestrial region. To further understand this phenomenon, here we present the discovery of four new EDDs. By complementing them with four recently identified systems from the literature we perform multi-band mid-IR photometry on the whole sample with the VLT/VISIR camera to examine whether they exhibit solid-state features around 10 μm.

Our new findings bring the EDD sample to 24. For the four new discoveries and one additional object, we provide a detailed analysis of the properties of the hosts stars and the discs. Based on the age estimates, we find that J104416, one of the newly identified systems, is probably the oldest known EDD with its age of ~5.5 Gyr.

The obtained photometry at 8.7, 10.7, and 12.4 μm implies that all eight targets likely exhibit distinct 10 μm feature. This further strenghtens the previously recognized trend that EDDs tend to display prominent solid-state features, indicative of abundant sub-micron-sized dust grains. Considering our new results, out of the 19 systems where this characteristic could be examined, this is true for 18. As mid-IR spectroscopic studies of previously known EDDs showed, the majority of them have 8–13 μm spectra charaterized by strong features peaking between 9.9 and 11.3 μm, suggesting dust material dominated by silicate particles, and only few show dominant feature peaks between 9 and 9.5 μm indicating the presence of silica grains. Based on the measured VISIR flux ratios, we have identified 4 discs in our sample that most probably belong to the silicate dominated subgroup. The classification of the other four objects is less certain, nevertheless, two of them may contain some silica.

As light curves at 3–5 μm show, mid-IR variability on yearly timescales is a common property of EDDs. We concluded that the variability level of discs belonging to the silicate-rich group is typically higher than that of silica-bearing systems. Meng et al. (2015) found similar results using a smaller sample of EDDs. This seems somewhat surprising, given that both the variability and the silica formation are thought to be due to the aftermath of high velocity collisions. It is possible, however, that silica dust can be formed in other ways (e.g., Lisse et al. 2020) and that the lifetime of the emerged silica material can be longer than the timescale of the processes leading to the mid-IR variability of the disc.

According to most current theories, EDDs are probably related to the accumulation of terrestrial planets, which is thought to be characterised by giant collisions between large planetary embryos. However, the age distribution we obtained for the 24 known systems strongly suggests that the formation of EDDs is unlikely to be limited to this process. While numerical simulations of the rocky planet formation and experiences in our Solar System imply that the vast majority of such giant impact events occur in the first 100 Myr, the incidence of EDDs begins to decrease only after 300 Myr and we know of a few objects older than 500 Myr as well. Remarkably, we have found that the majority of EDDs older than 100 Myr – at least 12 out of the 16 – are located in wide binary systems. Eccentricity constraints from Gaia astrometry are available for 7 of these binaries. For four of them, including the three oldest EDDs, the best eccentricity estimate is 0.99. For such eccentric orbits, even with large separations, it is conceivable that the companion star could have been able to significantly perturb the planetary system during its pericentre passage, triggering collisions among bodies located there. Such a late externally induced dynamical instability can provide a possible explanation for the formation of old EDDs. It is worth noting that in

the case of sufficiently high mutual inclination, the companion star can perturb substantially the orbital elements of the planetesimals and possible planets via the Kozai-Lidov mechanism, which can also trigger processes leading to significant dust production.

Future spectroscopic observations of these discs between 5 and 28 μm with the Mid-Infrared Instrument onboard the *James Webb Space Telescope* would allow their more detailed mineralogical analysis providing insights into the origin of their warm dust material.

ACKNOWLEDGEMENTS

We thank the referee for the constructive comments and suggestions that greatly improved the paper. This publication makes use of data products from the Wide-field Infrared Survey Explorer, which is a joint project of the University of California, Los Angeles, and the Jet Propulsion Laboratory/California Institute of Technology, and NEOWISE, which is a project of the JetPropulsion Laboratory/California Institute of Technology. WISE and NEOWISE are funded by the National Aeronautics and Space Administration. The publication makes use of data products from the Two Micron All Sky Survey, which is a joint project of the University of Massachusetts and the Infrared Processing and Analysis Center/California Institute of Technology, funded by the National Aeronautics and Space Administration and the National Science Foundation. This work has made use of data from the European Space Agency (ESA) mission *Gaia* (https://www.cosmos.esa.int/gaia), processed by the *Gaia* Data Processing and Analysis Consortium (DPAC, https://www.cosmos.esa.int/web/gaia/dpac/consortium). Funding for the DPAC has been provided by national institutions, in particular the institutions participating in the *Gaia* Multilateral Agreement. This research has made use of the NASA/ IPAC Infrared Science Archive, which is operated by the Jet Propulsion Laboratory, California Institute of Technology, under contract with the National Aeronautics and Space Administration. Based on observations collected at the European Organisation for Astronomical Research in the Southern Hemisphere under ESO programme(s) 090.C-0815 and 106.212F.001. We used the VizieR catalogue access tool and the Simbad object data base at CDS to gather data. This work was supported by the Hungarian National Research, Development and Innovation Office grants OTKA K131508 and the Élvonal grant KKP-143986. KV is supported by the Bolyai János Research Scholarship of the Hungarian Academy of Sciences and by the Bolyai+ grant ÚNKP-22-5-ELTE-1093. SM is supported by a Royal Society University Research Fellowship (URF-R1-221669). KYLSU acknowledges support from NASA ADAP programs (grant No. NNX17AF03G and 80NSSC20K1002).

DATA AVAILABILITY

The VISIR data used in this paper are publicly available at ESO Archive (http://archive.eso.org/eso/eso_archive_main.html).

REFERENCES

Almeida-Fernandes F., Rocha-Pinto H. J., 2018, MNRAS, 480, 4903
Bailer-Jones C. A. L., Rybizki J., Fouesneau M., Demleitner M., Andrae R., 2021, AJ, 161, 147
Ballering N. P., Rieke G. H., Gáspár A., 2014, ApJ, 793, 57
Barber M. G., Mann A. W., 2023, arXiv e-prints, p. arXiv:2302.09084
Barnes S. A., 2003, ApJ, 586, 464
Beichman C. A., et al., 2005, ApJ, 626, 1061
Beichman C. A., et al., 2011, ApJ, 743, 85
Bell C. P. M., Mamajek E. E., Naylor T., 2015, MNRAS, 454, 593
Belokurov V., et al., 2020, MNRAS, 496, 1922
Booth M., del Burgo C., Hambaryan V. V., 2021, MNRAS, 500, 5552
Bouma L. G., Palumbo E. K., Hillenbrand L. A., 2023, ApJ, 947, L3
Bouvier J., et al., 2018, A&A, 613, A63
Brahm R., Jordán A., Espinoza N., 2017a, PASP, 129, 034002
Brahm R., Jordán A., Hartman J., Bakos G., 2017b, MNRAS, 467, 971
Bryson S., Coughlin J., Batalha N. M., Berger T., Huber D., Burke C., Dotson J., Mullally S. E., 2020, AJ, 159, 279
Burnham K., Anderson D., 2002, Model selection and multimodel inference: a practical information-theoretic approach. Springer Verlag
Capitanio L., Lallement R., Vergely J. L., Elyajouri M., Monreal-Ibero A., 2017, A&A, 606, A65
Castelli F., Kurucz R. L., 2004, ArXiv Astrophysics e-prints,
Chambers K. C., et al., 2016, arXiv e-prints, p. arXiv:1612.05560
Chen C. H., et al., 2006, ApJS, 166, 351
Claytor Z. R., van Saders J. L., Santos Â. R. G., García R. A., Mathur S., Tayar J., Pinsonneault M. H., Shetrone M., 2020, ApJ, 888, 43
Cohen M., Walker R. G., Carter B., Hammersley P., Kidger M., Noguchi K., 1999, AJ, 117, 1864
Cotten T. H., Song I., 2016, ApJS, 225, 15
Cruz-Saenz de Miera F., Chavez M., Bertone E., Vega O., 2014, MNRAS, 437, 391
Cummings J. D., Deliyannis C. P., Maderak R. M., Steinhauer A., 2017, AJ, 153, 128
Curtis J. L., et al., 2020, ApJ, 904, 140
Cutri R. M., et al. 2014, VizieR Online Data Catalog, p. II/328
Cutri R. M., et al., 2003, VizieR Online Data Catalog, 2246
Czesla S., Schröter S., Schneider C. P., Huber K. F., Pfeifer F., Andreasen D. T., Zechmeister M., 2019, PyA: Python astronomy-related packages (ascl:1906.010)
Deacon N. R., Kraus A. L., 2020, MNRAS, 496, 5176
Dotter A., Chaboyer B., Jevremović D., Kostov V., Baron E., Ferguson J. W., 2008, ApJS, 178, 89
El-Badry K., Rix H.-W., Heintz T. M., 2021, MNRAS, 506, 2269
Fabricius C., et al., 2021, A&A, 649, A5
Fitton S., Tofflemire B. M., Kraus A. L., 2022, Research Notes of the American Astronomical Society, 6, 18
Fitzpatrick E. L., 1999, PASP, 111, 63
Freudling W., Romaniello M., Bramich D. M., Ballester P., Forchi V., García-Dabló C. E., Moehler S., Neeser M. J., 2013, A&A, 559, A96
Gagné J., Faherty J. K., 2018, ApJ, 862, 138
Gagné J., et al., 2018, ApJ, 856, 23
Gagné J., Faherty J. K., Moranta L., Popinchalk M., 2021, ApJ, 915, L29
Gaia Collaboration et al., 2023, A&A, 674, A1
Gorlova N., et al., 2004, ApJS, 154, 448
Gorlova N., Balog Z., Rieke G. H., Muzerolle J., Su K. Y. L., Ivanov V. D., Young E. T., 2007, ApJ, 670, 516
Hansen B. M. S., 2023, MNRAS, 520, 761
Henden A. A., Templeton M., Terrell D., Smith T. C., Levine S., Welch D., 2016, VizieR Online Data Catalog, 2336
Henning T., 2010, ARA&A, 48, 21
Higashio S., et al., 2022, ApJ, 933, 13
Høg E., et al., 2000, A&A, 357, 367
Houck J. R., et al., 2004, ApJS, 154, 18
Huang C. X., et al., 2020a, Research Notes of the American Astronomical Society, 4, 204
Huang C. X., et al., 2020b, Research Notes of the American Astronomical Society, 4, 206
Hwang H.-C., Ting Y.-S., Zakamska N. L., 2022a, MNRAS, 512, 3383
Hwang H.-C., El-Badry K., Rix H.-W., Hamilton C., Ting Y.-S., Zakamska N. L., 2022b, ApJ, 933, L32
Ishihara D., et al., 2010, A&A, 514, A1
Jackson A. P., Wyatt M. C., Bonsor A., Veras D., 2014, MNRAS, 440, 3757
Jeffries R. D., et al., 2023, MNRAS, 523, 802
Johnson B. C., et al., 2012, ApJ, 761, 45

Katz D., et al., 2023, A&A, 674, A5
Kaufer A., Stahl O., Tubbesing S., Nørregaard P., Avila G., Francois P., Pasquini L., Pizzella A., 1999, The Messenger, 95, 8
Kennedy G. M., Wyatt M. C., 2013, MNRAS, 433, 2334
Kennedy G. M., et al., 2014, MNRAS, 438, 3299
Kennedy G. M., Kenworthy M. A., Pepper J., Rodriguez J. E., Siverd R. J., Stassun K. G., Wyatt M. C., 2017, Royal Society Open Science, 4, 160652
Kennedy G. M., et al., 2020, MNRAS, 496, L75
Kerr R., Kraus A. L., Murphy S. J., Krolikowski D. M., Bedding T. R., Rizzuto A. C., 2022, ApJ, 941, 143
Kochanek C. S., et al., 2017, PASP, 129, 104502
Koike C., Noguchi R., Chihara H., Suto H., Ohtaka O., Imai Y., Matsumoto T., Tsuchiyama A., 2013, ApJ, 778, 60
Kounkel M., Covey K., 2019, AJ, 158, 122
Kounkel M., Covey K., Stassun K. G., 2020, AJ, 160, 279
Kunimoto M., et al., 2021, Research Notes of the American Astronomical Society, 5, 234
Kunimoto M., Tey E., Fong W., Hesse K., Shporer A., Fausnaugh M., Vanderspek R., Ricker G., 2022, Research Notes of the American Astronomical Society, 6, 236
Lagage P. O., et al., 2004, The Messenger, 117, 12
Lallement R., Vergely J.-L., Valette B., Puspitarini L., Eyer L., Casagrande L., 2014, A&A, 561, A91
Lallement R., et al., 2018, A&A, 616, A132
Lebouteiller V., Barry D. J., Spoon H. W. W., Bernard-Salas J., Sloan G. C., Houck J. R., Weedman D. W., 2011, ApJS, 196, 8
Lewis T., Watt L., Leinhardt Z. M., 2023, MNRAS, 519, 172
Lindegren L., et al., 2021, A&A, 649, A2
Lisse C. M., Chen C. H., Wyatt M. C., Morlok A., 2008, ApJ, 673, 1106
Lisse C. M., Chen C. H., Wyatt M. C., Morlok A., Song I., Bryden G., Sheehan P., 2009, ApJ, 701, 2019
Lisse C. M., et al., 2012, ApJ, 747, 93
Lisse C. M., et al., 2020, ApJ, 894, 116
Mann A. W., Feiden G. A., Gaidos E., Boyajian T., von Braun K., 2015, ApJ, 804, 64
Mannings V., Barlow M. J., 1998, ApJ, 497, 330
Markwardt C. B., 2009, in Bohlender D. A., Durand D., Dowler P., eds, Astronomical Society of the Pacific Conference Series Vol. 411, Astronomical Data Analysis Software and Systems XVIII. p. 251 (arXiv:0902.2850)
Melis C., 2016, in Kastner J. H., Stelzer B., Metchev S. A., eds, Vol. 314, Young Stars & Planets Near the Sun. pp 241–246 (arXiv:1509.05726), doi:10.1017/S1743921315006638
Melis C., Zuckerman B., Rhee J. H., Song I., 2010, ApJ, 717, L57
Melis C., Zuckerman B., Rhee J. H., Song I., Murphy S. J., Bessell M. S., 2012, Nature, 487, 74
Melis C., Olofsson J., Song I., Sarkis P., Weinberger A. J., Kennedy G., Krumpe M., 2021, ApJ, 923, 90
Meng H. Y. A., et al., 2014, Science, 345, 1032
Meng H. Y. A., et al., 2015, ApJ, 805, 77
Mittal T., Chen C. H., Jang-Condell H., Manoj P., Sargent B. A., Watson D. M., Lisse C. M., 2015, ApJ, 798, 87
Moór A., et al., 2021, ApJ, 910, 27
Moór A., et al., 2022, MNRAS, 516, 5684
Moore N. W. H., Li G., Hassenzahl L., Nesvold E. R., Naoz S., Adams F. C., 2023, ApJ, 943, 6
Moranta L., Gagné J., Couture D., Faherty J. K., 2022, ApJ, 939, 94
Morlok A., Mason A. B., Anand M., Lisse C. M., Bullock E. S., Grady M. M., 2014, Icarus, 239, 1
Moshir M., Kopman G., Conrow T. A. O., 1992, IRAS Faint Source Survey, Explanatory supplement version 2
Naoz S., 2016, ARA&A, 54, 441
Nesvold E. R., Naoz S., Vican L., Farr W. M., 2016, ApJ, 826, 19
Neugebauer G., et al., 1984, ApJ, 278, L1
Olofsson J., Juhász A., Henning T., Mutschke H., Tamanai A., Moór A., Ábrahám P., 2012, A&A, 542, A90
Oudmaijer R. D., van der Veen W. E. C. J., Waters L. B. F. M., Trams N. R., Waelkens C., Engelsman E., 1992, A&AS, 96, 625
Pecaut M. J., Mamajek E. E., 2013, ApJS, 208, 9
Pecaut M. J., Mamajek E. E., 2016, MNRAS, 461, 794
Popinchalk M., Faherty J. K., Kiman R., Gagné J., Curtis J. L., Angus R., Cruz K. L., Rice E. L., 2021, ApJ, 916, 77
Quintana E. V., Barclay T., Borucki W. J., Rowe J. F., Chambers J. E., 2016, ApJ, 821, 126
Reddy B. E., Lambert D. L., Allende Prieto C., 2006, MNRAS, 367, 1329
Rhee J. H., Song I., Zuckerman B., 2008, ApJ, 675, 777
Ricker G. R., et al., 2015, Journal of Astronomical Telescopes, Instruments, and Systems, 1, 014003
Rieke G. H., Su K. Y. L., Melis C., Gáspár A., 2021, ApJ, 918, 71
Riello M., et al., 2021, A&A, 649, A3
Rigley J. K., Wyatt M. C., 2022, MNRAS, 510, 834
Sankar S., Melis C., Klein B. L., Fulton B. J., Zuckerman B., Song I., Howard A. W., 2021, ApJ, 922, 75
Schneider A. C., Shkolnik E. L., Allers K. N., Kraus A. L., Liu M. C., Weinberger A. J., Flagg L., 2019, AJ, 157, 234
Sestito P., Randich S., 2005, A&A, 442, 615
Shappee B. J., et al., 2014, ApJ, 788, 48
Silverberg S. M., et al., 2018, ApJ, 868, 43
Skrutskie M. F., et al., 2006, AJ, 131, 1163
Sokolovsky K. V., et al., 2017, MNRAS, 464, 274
Song I., Zuckerman B., Weinberger A. J., Becklin E. E., 2005, Nature, 436, 363
Su K. Y. L., et al., 2019, AJ, 157, 202
Su K. Y. L., Rieke G. H., Melis C., Jackson A. P., Smith P. S., Meng H. Y. A., Gáspár A., 2020, ApJ, 898, 21
Su K. Y. L., Kennedy G. M., Schlawin E., Jackson A. P., Rieke G. H., 2022, ApJ, 927, 135
Su K. Y. L., et al., 2023, arXiv e-prints, p. arXiv:2310.12336
Tajiri T., et al., 2020, ApJS, 251, 18
Tokovinin A., Briceño C., 2020, AJ, 159, 15
Tonry J. L., et al., 2012, ApJ, 750, 99
Torres C. A. O., Quast G. R., Melo C. H. F., Sterzik M. F., 2008, Young Nearby Loose Associations. p. 757
Ujjwal K., Kartha S. S., Mathew B., Manoj P., Narang M., 2020, AJ, 159, 166
Vican L., Schneider A., Bryden G., Melis C., Zuckerman B., Rhee J., Song I., 2016, ApJ, 833, 263
Watt L., Leinhardt Z., Su K. Y. L., 2021, MNRAS, 502, 2984
Weinberger A. J., 2008, ApJ, 679, L41
Werner M. W., et al., 2004, ApJS, 154, 1
Wolniewicz L. M., Berger T. A., Huber D., 2021, AJ, 161, 231
Woo J. M. Y., Brasser R., Grimm S. L., Timpe M. L., Stadel J., 2022, Icarus, 371, 114692
Wood M. L., et al., 2023, arXiv e-prints, p. arXiv:2310.16883
Wright E. L., et al., 2010, AJ, 140, 1868
Wyatt M. C., 2008, ARA&A, 46, 339
Wyatt M. C., Smith R., Greaves J. S., Beichman C. A., Bryden G., Lisse C. M., 2007, ApJ, 658, 569
Young S. D., Wyatt M. C., 2023, MNRAS,
Zechmeister M., Kürster M., 2009, A&A, 496, 577
Zuckerman B., 2015, ApJ, 798, 86
Zuckerman B., Fekel F. C., Williamson M. H., Henry G. W., Muno M. P., 2008, ApJ, 688, 1345
Zuckerman B., Melis C., Rhee J. H., Schneider A., Song I., 2012, ApJ, 752, 58
da Silva L., Torres C. A. O., de La Reza R., Quast G. R., Melo C. H. F., Sterzik M. F., 2009, A&A, 508, 833
de Wit W. J., Grinin V. P., Potravnov I. S., Shakhovskoi D. N., Müller A., Moerchen M., 2013, A&A, 553, L1
Žerjal M., Ireland M. J., Crundall T. D., Krumholz M. R., Rains A. D., 2023, MNRAS, 519, 3992

APPENDIX A: MEMBERSHIP OF J071206 IN THE CRIUS 228 MOVING GROUP

By analyzing the Galactic space positions and velocities of Gaia Early Data Release 3 stars located within 200 pc using the HDBSCAN unsupervised clustering algorithm, Moranta et al. (2022) have identified 241 stellar clusters. As Figure A1 (top panels) demonstrates the location and motion of J071206 are similar to those of the Crius 228 group members: it is located 36.2 pc from the centre of the group and its space velocity components are U=−6.0±0.1 km s^{-1}, V=−24.6±0.1 km s^{-1}, and W=−15.1±0.2 km s^{-1} (see Table 2), while the characteristic UVW velocities of the group are −7.5 km s^{-1}, −24.7 km s^{-1}, and −14.1 km s^{-1}, respectively.

To estimate the age of the Crius 228, we used gyrochronology by employing the recent calibration proposed by Bouma et al. (2023). To use the latter method, we need to know the effective temperatures and rotation periods of the stars. The $T_{\rm eff}$ parameters were estimated from the dereddened Gaia $(Bp - Rp)_0$ colour indices by adopting the conversion from Curtis et al. (2020). Based on the Stilism 3D extinction map[15] (Lallement et al. 2014; Capitanio et al. 2017), we found that only one of the targets has non-negligible reddening. Since the applied gyrochronal model is validated for stars with $T_{\rm eff}$ between 3800 K and 6200 K (Bouma et al. 2023), we removed all targets with temperatures out of this interval from the sample. Two additional stars, where the `ruwe` values of >1.2 indicate possible binarity, were also removed, as the presence of a nearby pair may affect their colour index, and hence the $T_{\rm eff}$ estimate. To determine the rotation period of the remaining fifteen targets, we analyzed their TESS light curves following the method described in Sect. 2.5. These objects were measured in 2 to 13 TESS sectors, with data from 4 to 6 sectors for most. Finally, we found 11 cases with well-defined periodic rotational modulation, the data of which are summarized in Table A1. Figure A1 (bottom left panel) shows the derived rotation periods as a function of $T_{\rm eff}$ for Crius 228 members as well as for well dated clusters with ages between 120 and 670 Myr for comparison. The majority of Crius 228 stars constitute a quite narrow sequence in between the loci of the ∼120 Myr old Pleiades/Blanco I/Psc-Eri and the 300 Myr old Group X/NGC 3521 groups, suggesting an age of 200–250 Myr. To provide a more quantitative age estimate, we used the `gyro-interp` tool (Bouma et al. 2023) to derive age posteriors for each member using their $T_{\rm eff}$ and $P_{\rm rot}$ parameters, and then we determined the age posterior of the group by combining the individual ones (Figure A1, bottom right panel). This yields an age estimate of 231±35 Myr for Crius 228. As shown in Fig. A1 (bottom panels) – assuming that the rotation period obtained for J071206 is associated with the primary component, and not to the putative secondary – then this object fits very well with the rotation sequence of Crius 228 members giving an additional indication of its membership.

Using the excess photometric uncertainty in Gaia photometry as a proxy for variability, Barber & Mann (2023) found that the distribution of their variability parameter (the 90th percentile of the values) defined in this way for a stellar association correlates well with the age of the group and can thus be used for age diagostics. Though this method work best for groups with >100 members, by applying it for the relatively small Crius 228 using the EVA tool[16], we obtained an age estimate of 260^{+68}_{-46} Myr, which is good accordance with the gyrochrone age. Moranta et al. (2022) proposed that the Crius 228 possibly constitute a subset of the Theia 301 association (Kounkel & Covey 2019). For the latter group, Kounkel et al. (2020) derived an isochronal age of 195^{+87}_{-60} Myr, which is also consistent with both of the above estimates. On the other hand, Gagné et al. (2021) argued that Theia 301 may form a trailing tidal tail behind the Pleiades open cluster and has an age of ∼110 Myr.

Further investigations are needed to see how Crius 228 and Theia 301 relate to each other and whether the latter is a single entity or a mixture of several clusters of different ages. The member list proposed by Moranta et al. (2022) for Crius 228 is based on the Gaia EDR3 catalogue. In the new DR3 database, radial velocity data are available for many more objects, the analysis of which may help to clarify the above question and possibly lead to the identification of additional Crius 228 members thereby providing the opportunity to further refine the age of the group. Such a study, however, is out of the scope of the present work.

Table A1. Rotation periods for Crius 228 members

Gaia DR3 name	$T_{\rm eff}$	$P_{\rm rot}$	TESS Sectors
2884927509794635392	4209	5.57±0.02	32,33
2885816980343235968	5932	5.23±0.21	6,32,33
2890261206342983680	5122	7.19±0.38	5,6,32,33
5502604317431258624	5655	4.47±0.10	5,6,7,8,32,33,34,35
5504497161061675648	5838	3.66±0.09	6,7,8,33,34,35
5507915130394590592	5979	3.12±0.14	6,7,8,33,34,35
5551398959847312640	4529	9.80±0.60	6,7,8,33,34
5553080555504933120	4764	8.73±0.28	5,7,28,32,33,34
5555858785167602432	5586	5.62±0.15	6,7,33,34
5566867125647181568	5036	7.57±0.12	5,7,32,33,34
5566896748038703488	5182	6.93±0.12	5,7,32,33,34

APPENDIX B: NEOWISE W1 AND W2 LIGHT CURVES OF RECENTLY IDENTIFIED EDDS

In this section, we present light curves showing how the *WISE W*1 and *W*2 band disc fluxes of seven EDDs (J060917, J071206, J092521, J104416, J204315, J045959, and TYC 8830) were changed on yearly timescale between 2013 and 2022.

APPENDIX C: THE LIST OF CURRENTLY KNOWN EDDS

[15] https://stilism.obspm.fr/
[16] https://github.com/madysonb/EVA

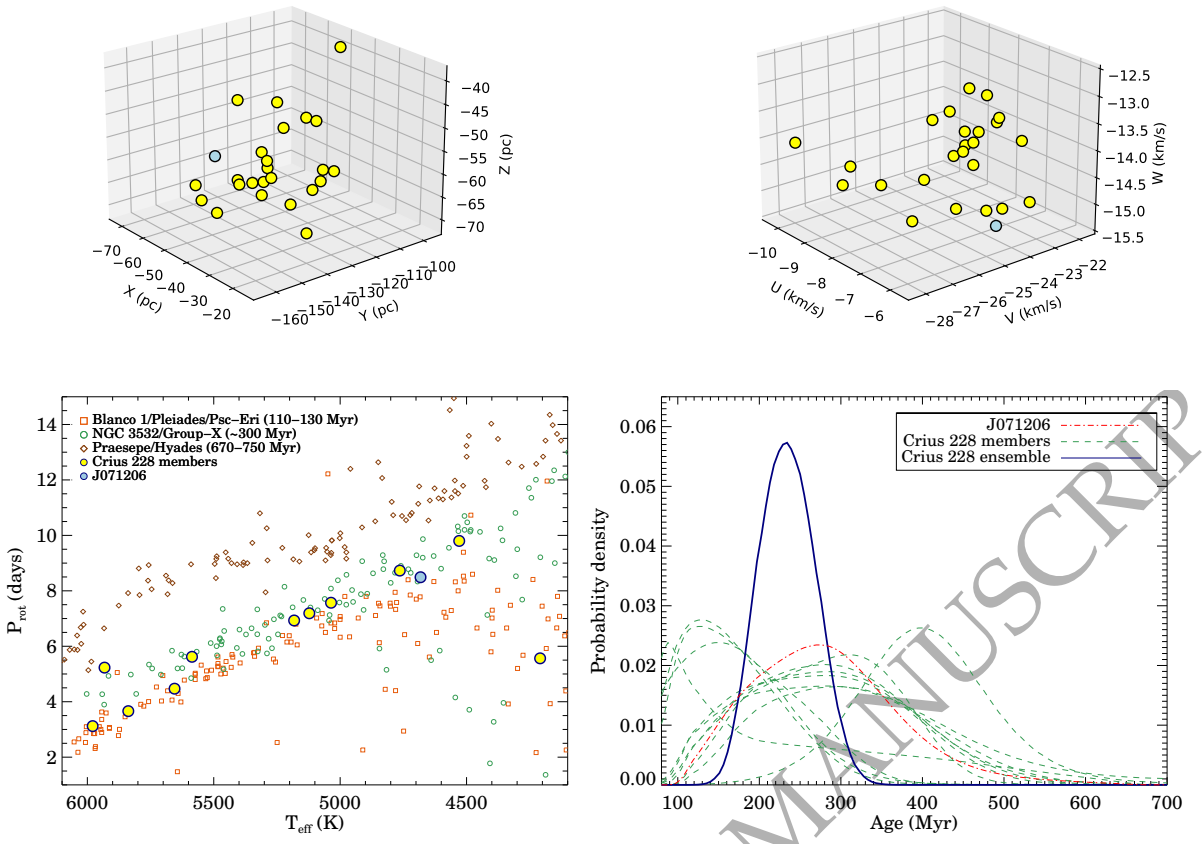

Figure A1. Top panels: the X, Y, and Z galactic coordinates (left) and U, V, and W galatic space velocity components (right) of Crius 228 members (Moranta et al. 2022) with `ruwe` <1.2 (yellow circles) and J071206 (blue circle). Bottom panel, left: rotation periods of Crius 228 members and J071206 as a function of $T_{\rm eff}$. For comparison $T_{\rm eff}$-$P_{\rm rot}$ distributions of 6 stellar groups are also displayed. The latter data were taken from Bouma et al. (2023). Bottom panel, right: age posteriors for individual stars from gyrochronology analysis performed by the `gyro-interp` tool.

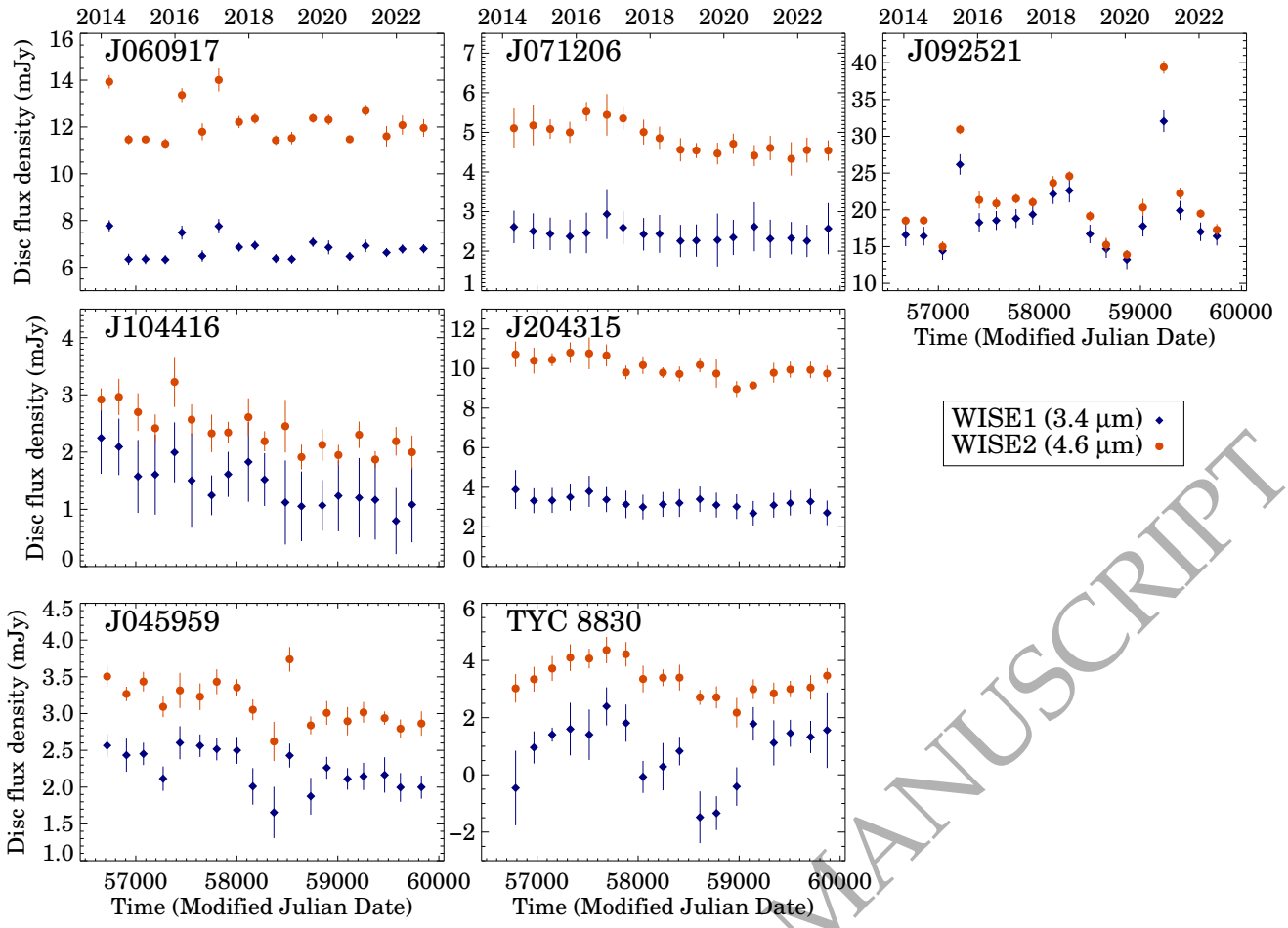

Figure B1. Disc flux data (the measured excess emissions) of the five EDDs analysed in Sect. 2 (top five panels) and two other recently identified EDDs (bottom two panels) in the *WISE* $W1$ and $W2$ bands from 2013 to 2022 during the NEOWISE Reactivation mission. The displayed light curves have a cadence of ~180 days and their data points are derived by averaging the available good quality single exposure measurements in each observing window (Sect. 2.7.3).

Table C1. List of known EDDs. References for discovery papers: 1 - de Wit et al. (2013); 2 - Gorlova et al. (2004); 3 - Gorlova et al. (2007); 4 - Higashio et al. (2022); 5 - Mannings & Barlow (1998); 6 - Melis et al. (2012); 7 - Melis et al. (2021); 8 - Moór et al. (2021); 9 - Oudmaijer et al. (1992); 10 - Rhee et al. (2008); 11 - Song et al. (2005); 12 - Tajiri et al. (2020); 13 - Zuckerman et al. (2012); 14 - This paper.

Short ID[a]	AllWISE ID	Simbad ID	Discovery
RZ Psc	J010942.07+275701.7	V* RZ Psc	1
BD+20 307	J015450.37+211822.2	BD+20 307	11
HD 15407	J023050.76+553253.3	HD 15407	9
V488 Per	J032818.69+483947.9	V* V488 Per	13
HD 23514	J034638.40+225510.7	HD 23514	10
J045959	J045959.96-084136.7	TIC 43488669	12
TYC 4515	J050407.19+775857.1	TYC 4515-485-1	8
TYC 5940	J060513.59-191308.4	TYC 5940-1510-1	8
J060917	J060917.00-150808.5	-	14
TYC 8105	J061103.54-471129.2	TYC 8105-370-1	8
J071206	J071206.54-475242.3	-	14
P1121	J073542.68-145042.2	Cl* NGC 2422 PMS 1121	2
ID8	J080902.49-485817.2	[GBR2007] ID 8	3
J092521	J092521.90-673224.8	TYC 9196-2916-1	4
J104416	J104416.70-451613.9	CD-44 6765	14
TYC 8241	J120902.21-512041.0	TYC 8241-2652-1	6
TYC 4946	J121334.13-053543.4	TYC 4946-1106-1	8
HD 113766	J130635.75-460202.1	HD 113766	9
HD 145263	J161055.09-253121.9	HD 145263	5
HD 166191	J181030.32-233400.5	HD 166191	9
TYC 4209	J181703.92+643354.9	TYC 4209-1322-1	8
J204315	J204315.23+104335.3	-	14
TYC 8830	J230112.67-585821.9	TYC 8830-410-1	7
TYC 4479	J235250.65+673037.2	TYC 4479-3-1	8

[a] Short identifiers of EDDs using throughout the paper.